IVYSPRING INTERNATIONAL PUBLISHER

Theranostics

2027; 17(1): 604-626. doi: 10.7150/thno.140120

Research Paper

# Z-Scheme interface engineering in bimetallic sulfide sonozymes to dismantle tumor antioxidant defenses for ferroptosis-driven sono-immunotherapy

Yang Yang[1*], Xiuwei Wu[1*], Zhenlin Zhang[2], Dengyu Pan[2], Bijiang Geng[2✉], Yunsheng Cheng[3✉]

1. Department of Oncology, The Second Affiliated Hospital of Anhui Medical University, Hefei, Anhui 230601, China.
2. School of Environmental and Chemical Engineering, Shanghai University, Shanghai 200444, China.
3. Department of General Surgery, Second Affiliated Hospital of Anhui Medical University, Hefei, Anhui 230601, China.

* These authors contributed equally to this work.

✉ Corresponding authors: E-mail addresses: bjgeng1992@shu.edu.cn (B. Geng); chengyunsheng@ahmu.edu.cn (Y. Cheng).

© 2027 The Author(s). This is an open access article distributed under the Creative Commons Attribution 4.0 International Licence, subject to the Publisher's Terms of Use at https://ivyspring.com/terms.

Received: 2026.06.30; Accepted: 2026.09.25; Published: 2027.01.01

## Abstract

**Background:** Although sonodynamic therapy (SDT) has great potential for precise treatment of malignant tumors, its efficacy is severely hindered by the complex tumor microenvironment (TME), characterized by hypoxia and high levels of glutathione (GSH), as well as rapid recombination of sono-generated carriers.

**Methods:** We design a Z-scheme CD@$FeV_2S_4$ heterojunction sonozyme by anchoring zero-dimensional carbon dots (CDs) onto bimetallic sulfide $FeV_2S_4$ nanocubes, achieving the cascade amplification of anti-tumor immune response. In the sonozyme system, $FeV_2S_4$ exhibits multienzyme-mimic activities (CAT, POD, and GSH-ox) to alleviate tumor hypoxia and consume endogenous GSH, effectively breaking down the antioxidant defense barrier within tumors. The Z-scheme charge transfer mechanism of CD@$FeV_2S_4$ heterojunctions significantly suppresses electron-hole recombination and triggers a ROS storm.

**Results:** The synergistic TME remodeling and ROS production induce severe lipid peroxidation and ferroptosis, accompanied by downregulation of GPX4 and SLC7A11. It is crucial that CD@$FeV_2S_4$ heterojunctions-mediated cascade-amplified ROS production and ferroptosis strongly trigger immunogenic cell death, promote dendritic cell maturation, and ultimately activate T cells.

**Conclusion:** *In vivo* experiments using bilateral tumor models have demonstrated that CD@$FeV_2S_4$-mediated combination therapy can eradicate primary tumors and awaken the systemic adaptive immune response, exerting a strong inhibitory effect on distant metastatic tumors. This work provides a distinct paradigm for designing efficient Z-scheme heterojunction sonozymes to overcome local immune tolerance and achieve systemic distant anti-tumor effects.

Keywords: carbon dots, sonozymes, ferroptosis, sonodynamic therapy, immunotherapy

## Introduction

Malignant tumors are one of the major diseases that seriously threaten human health [1-3]. Their high incidence rate and mortality make it a huge challenge for global public health [4, 5]. Traditional clinical interventions such as surgery, radiotherapy, and chemotherapy, although improving patient prognosis, often come with inevitable limitations [6, 7]. For example, surgery is difficult to completely remove small metastases [8, 9], while radiotherapy and chemotherapy inevitably cause serious systemic toxic side effects [10], are prone to drug resistance, and have limited efficacy for deep solid tumors [11, 12]. To overcome the bottlenecks of these traditional therapies, a new non-invasive tumor treatment strategy based on reactive oxygen species (ROS) has emerged [13-17]. Sonodynamic therapy (SDT) has shown great potential for clinical translation in the field of precision cancer treatment due to its extremely high tissue penetration depth, non-invasiveness, and excellent spatiotemporal targeting controllability [18-21]. SDT mainly relies on low-frequency ultrasound (US) to excite sonosensitizers that accumulated at the

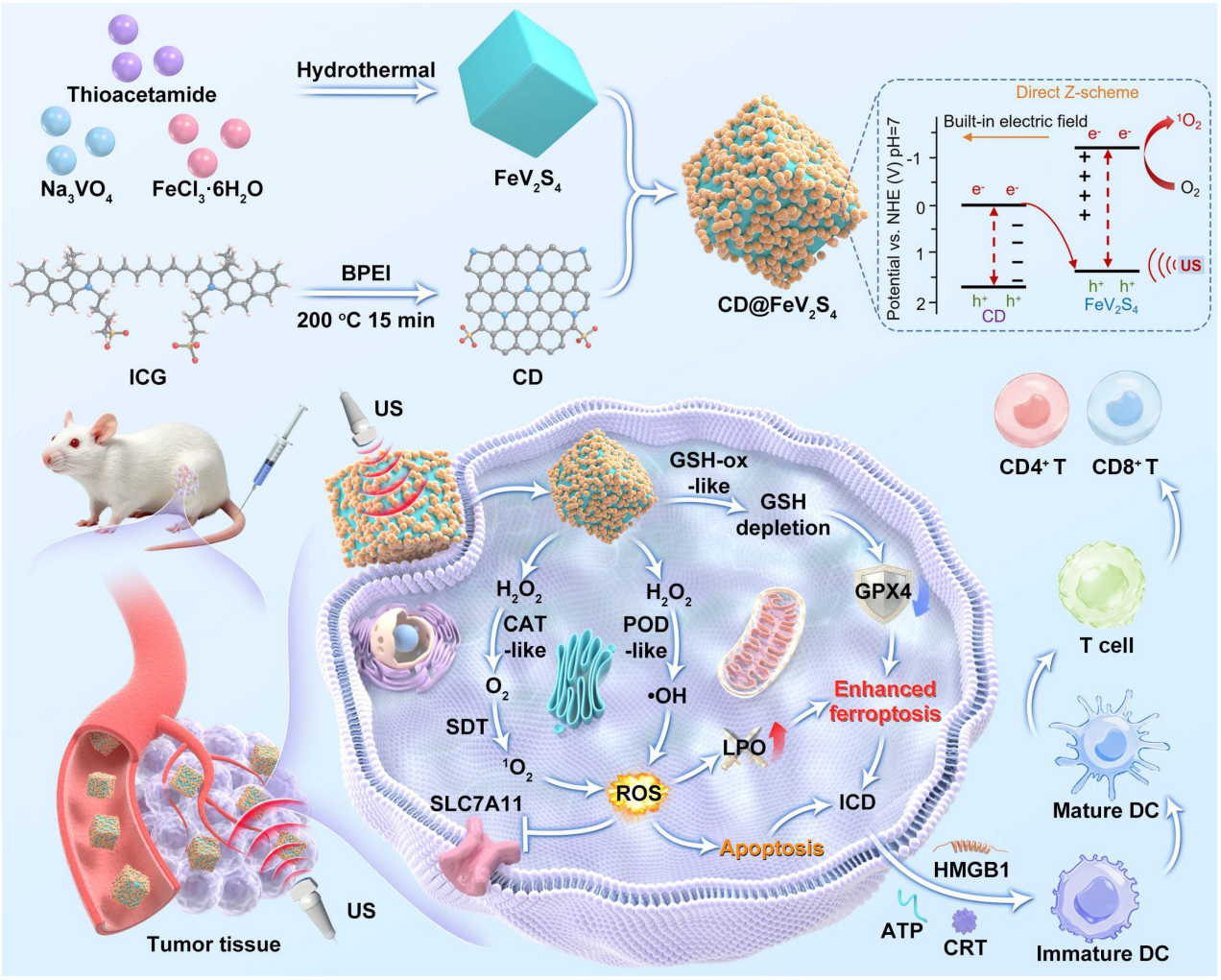
tumor site, promoting the production of highly toxic ROS, irreversibly destroying macromolecules and inducing tumor cell apoptosis [22-24]. However, the complex tumor microenvironment (TME) characteristics of solid tumors greatly limit the treatment efficacy of single SDT [25-27]. TME typically exhibits severe hypoxia [27, 28], overexpression of glutathione (GSH) [29, 30], and micro-acidity. On the one hand, the abnormal vascular network and rapid cell proliferation within solid tumors lead to severe hypoxia, directly cutting off the source of oxygen substrates for ROS generation during SDT process [31]. On the other hand, the abnormally elevated GSH in tumor cells, as an endogenous antioxidant, can significantly consume the generated ROS, forming a strong antioxidant defense barrier [29, 30, 32]. Therefore, how to effectively remodel TME and break the endogenous antioxidant defense mechanism of tumors is a key bottleneck that urgently needs to be solved to improve the SDT efficacy.

To overcome the severe challenges brought by TME, utilizing nanozyme-mediated nanocatalytic therapy (NCT) to reshape TME and generate active free radicals *in situ* has become a highly promising strategy [33-35]. Nanozymes with multiple enzyme-mimic activities can utilize the specific microenvironment within tumors for *in situ* catalytic reactions. For example, its CAT-like activity can catalyze the decomposition of overexpressed $H_2O_2$ in tumors to produce oxygen, effectively alleviating hypoxia [36]. The activity of GSH-oxidase-like (GSH-ox-like) can specifically deplete the excessive accumulation of GSH and break down the antioxidant barrier of tumors [37]. More importantly, its POD-like activity can directly convert $H_2O_2$ into highly toxic •OH through a Fenton/Fenton-like reaction [38]. Therefore, combining the TME regulation and endogenous catalytic ability of nanozymes with the exogenous US response characteristics of sonosensitizers to develop a sonozyme system that integrates nanozyme functions and sonosensitizer activity is considered a promising strategy to achieve cascade amplification of ROS production. However, the therapeutic effect of sonozymes is still greatly constrained, mainly due to two challenges. First, the enzymatic catalytic activity of single metal based nanomaterials is often limited, making it difficult to achieve efficient catalytic conversion in slightly acidic TME [39-41]. Second, the electron-hole pairs generated by conventional sonosensitizers under US excitation are prone to rapid recombination, leading to a low quantum yield of ROS induced by SDT [42, 43]. To solve this dual dilemma, constructing a band-matched Z-scheme heterojunction with unique interface charge transfer mechanism can not only greatly suppresses the recombination of active carriers, but also retains the electrons and holes with the strongest oxidation and reduction potentials in the two components [44, 45]. The electronic structure rearrangement of this interface maximizes the efficiency of US-activated ROS generation and synergistically enhance the catalytic activity of nanozymes [46].

It is worth emphasizing that the fabricated Z-scheme heterojunctions can not only significantly enhance the sonozyme catalytic efficiency of a single component, but more importantly, the ROS cascade amplification effect triggered by heterojunction sonozymes can trigger robust anti-tumor immune responses [47, 48]. In addition to triggering apoptosis of tumor cells, ROS storm can also cause oxidative stress damage and effectively induce immunogenic cell death (ICD), which is accompanied by exposure to a large number of damage-related molecular patterns (DAMPs) to promote the maturation of dendritic cells (DCs) and the activation of T lymphocytes [49, 50]. Furthermore, ROS storm mediated by heterojunction sonozymes combined with GSH depletion can disrupt the antioxidant defense network of tumor cells, irreversibly trigger lipid peroxidation, and subsequently induce ferroptosis [51]. Recent studies have confirmed that ferroptosis has high immunogenicity and can produce a synergistic amplification effect with the ICD, further enhancing antigen presentation and awakening anti-tumor immunity [52]. Therefore, utilizing Fe-based sonozymes as the heterojunction component could not only serve as an active site for Fenton reactions to maintain sustained ROS production, but also directly participate in ferroptosis and accelerate lipid peroxidation processes. This design is expected to achieve a multiple cascade response mechanism of ROS cascade amplification, ferroptosis induction, and ICD initiation co-enhanced systemic immune activation under US stimulation, providing driving force for the complete eradication of primary tumors and inhibition of distant tumors.

Quasi-zero-dimensional carbon dots (CDs), as an emerging non-metallic nanomaterial, have attracted much attention in the biomedical field due to their excellent biocompatibility and photo/sono physicochemical properties [17, 53]. It is worth mentioning that the band structure and surface interface characteristics of CDs can be precisely controlled by adjusting surface functional groups [17, 54]. This unique advantage makes it not only an efficient sonosensitizers with the ability to generate ROS mediated by triplet states, but also an ideal electronic medium for achieving band matching with metal-based sonozymes and constructing efficient Z-type heterojunctions. In this work, we utilized CD

sonosensitizers to sensitize $FeV_2S_4$ sonozymes for the fabrication of TME-responsive CD@$FeV_2S_4$ Z-scheme heterojunction sonozymes, which were employed to realize the cascade amplification of antitumor immune response. Specifically, we first synthesized a bimetallic sulfide $FeV_2S_4$ sonozyme with a uniform nanocube morphology, which exhibited excellent multiple enzyme-mimic activity (POD-like, CAT-like, and GSH-ox-like activities) for the remission of hypoxia and antioxidant barriers of TME. Then, negatively charged CD sonosensitizers were anchored to the positively charged $FeV_2S_4$ sonozyme surface through electrostatic adsorption, constructing a Z-scheme heterojunction with a tight interface. Under US excitation, the Z-scheme charge transfer mechanism greatly suppresses the recombination of sono-generated carriers, resulting in the production of massive amounts of ROS in tumor tissues. *In vitro* and *in vivo* experiments have confirmed that the cascade amplification of ROS production, driven by TME remodeling and a strong ROS storm, induces lipid peroxidation and ferroptosis in tumor cells (accompanied by significant downregulation of key proteins GPX4 and SLC7A11). More importantly, this cellular destruction strongly triggers immunogenic cell death (ICD), releasing a large number of DAMPs. In the bilateral tumor model, the synergistic therapy mediated by CD@$FeV_2S_4$ Z-scheme heterojunction sonozymes effectively promotes the maturation of DCs while successfully eliminating primary tumors, and awakens systemic T cell-mediated anti-tumor immunity (significant infiltration of $CD8^+$ T cells), thereby achieving strong inhibition of distant metastasis without US irradiation. This work not only provides a new approach for designing efficient Z-scheme sonosensitizer heterojunction based on nanozymes, but also offers a highly promising paradigm for overcoming local immune resistance in tumors and achieving systemic distant anti-tumor effects.




**Scheme 1.** Schematic diagram for the fabrication of a TME-responsive CD@$FeV_2S_4$ Z-scheme heterojunction sonozymes for tumor immunotherapy through depositing CD sonosensitizers on $FeV_2S_4$ sonozymes. The Z-scheme charge transfer mechanism greatly suppresses the recombination of sono-generated carriers and amplifies the ROS production. The amplification effect of ROS generation combined with ferroptosis can induce ICD, facilitate the maturation of DC, and awaken systemic T cell-mediated anti-tumor immunity.

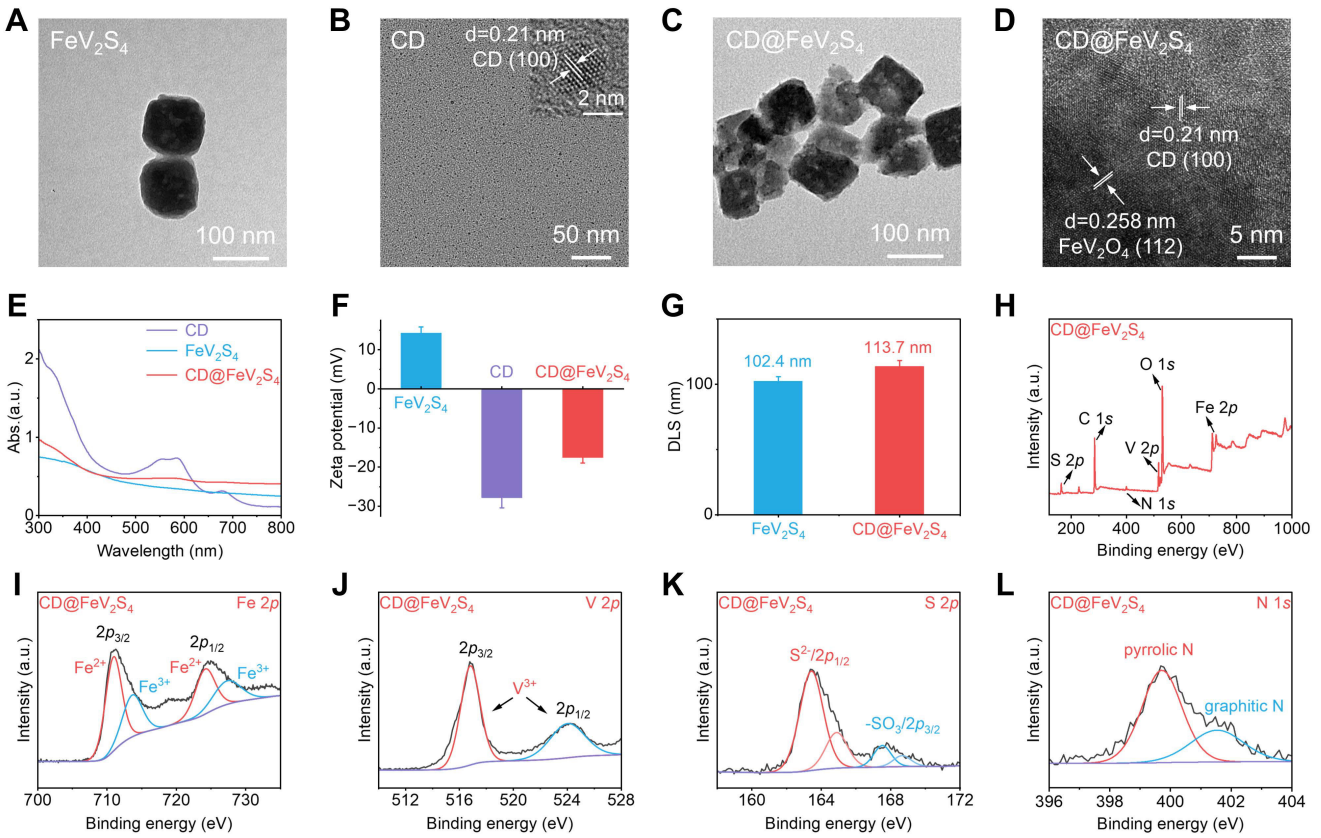



**Figure 1.** (A) TEM images of $FeV_2S_4$ and $CD@FeV_2S_4$. (B) TEM and HR-TEM (inset) of CDs. (C) TEM images of $CD@FeV_2S_4$. (D) HR-TEM of $CD@FeV_2S_4$. (E) Absorption spectra of CD, $FeV_2S_4$ and $CD@FeV_2S_4$. (F) Zeta potential of $FeV_2S_4$, CD, and $CD@FeV_2S_4$. (G) Hydrodynamic diameter of $FeV_2S_4$ and $CD@FeV_2S_4$. (H-L) Survey XPS (H), high-resolution Fe 2*p* (I), V 2*p* (J), S 2*p* (K) and N 1*s* (L) spectra of $CD@FeV_2S_4$. Data are presented as the mean ± SD. (n = 3).

## Results and Discussion

$CD@FeV_2S_4$ Z-Scheme heterojunction was synthesized as illustrated in Scheme 1, where zero-dimensional CDs were loaded onto the surface of the binary metal sulfide $FeV_2S_4$ via a two-step method, forming a composite structure with tight interfacial contact. Initially, $FeV_2S_4$ nanoparticles were successfully synthesized through a one-step hydrothermal process, employing thioacetamide, sodium vanadate, and ferric chloride as the sulfur (S), vanadium (V), and iron (Fe) sources, respectively. Transmission electron microscopy (TEM) characterization (Figure 1A) demonstrated that the obtained $FeV_2S_4$ exhibited a uniformly dispersed nano-cubic morphology, characterized by regular shapes, well-defined edges, and minimal agglomeration. The size distribution of these nanocubes is relatively narrow, centered around 100 nm, facilitating subsequent composite modifications. X-ray photoelectron spectroscopy (XPS) confirmed the co-existence of S, Fe, and V elements (Figure S1A). Further high-resolution spectral fitting revealed that Fe predominantly exists in +2 and +3 valence states (Figure S1B), as evidenced by the spin-orbit splitting peaks of Fe $2p_{3/2}$ and Fe $2p_{1/2}$, indicating mixed valence states within the material. V primarily exists in the +3 valence state (Figure S1C), with its V $2p_{3/2}$ binding energy located at approximately 516.2 eV, while S exists in the -2 valence state (Figure S1D). CDs with excellent triplet excited state-mediated sonodynamic activity were synthesized using the method we previously reported [17], the indocyanine green (ICG) and branched polyethylenimine (BPEI) were dissolved in anhydrous ethanol and rapidly synthesized via a one-step microwave method. TEM image illustrated in Figure 1B revealed that the synthesized CDs were uniformly dispersed with quasi-spherical in shape. The particle size distribution of CDs ranged from 2 to 5 nm and no significant aggregation can be detected in the CDs, implying their excellent dispersibility. High-resolution TEM further uncovered distinct lattice fringes with a spacing of 0.21 nm, which perfectly matched the (100) plane of graphitic carbon. This indicated that the CDs possess a graphene-like internal structure. XPS analysis confirmed the presence of S, C, N, and O elements in the CDs (Figure S2A). The sulfur element originates from the sulfonic acid group in the ICG molecule, while the nitrogen element comes from the amino group of BPEI. These heteroatom doping endow the CDs with abundant surface functional groups and a negative charge.

To form a CD@$FeV_2S_4$ Z-type heterojunction structure, we assembled negatively charged CDs onto the positively charged $FeV_2S_4$ surface via electrostatic adsorption (Figure 1F). Given that the CDs surface was rich in negatively charged groups such as sulfonate, its zeta potential was approximately -27.8 mV, while that of $FeV_2S_4$ was about +14.3 mV. This significant difference generates a strong electrostatic attraction, driving the CDs to tightly coat the $FeV_2S_4$ surface. TEM images clearly revealed dot-like CDs on the $FeV_2S_4$ surface (Figure 1C), uniformly attached to the edges and surfaces of the nano-cubes without noticeable agglomeration. Further observation of the composite's interface structure using HR-TEM revealed a 0.21 nm lattice spacing belonging to the CDs and a 0.258 nm lattice spacing attributed to $FeV_2S_4$, specifically its (112) crystal plane (Figure 1D). This confirms the successful formation of the CD@$FeV_2S_4$ composite structure, providing a structural foundation for the Z-type charge transfer pathway. A series of physicochemical characterizations were subsequently performed to validate the successful formation of CD@$FeV_2S_4$. Initially, we observed the spectral changes using UV-vis absorption spectroscopy. As depicted in Figure 1E, the absorption spectrum of $FeV_2S_4$ appeared as a horizontal straight line, whereas a significant alteration was observed in the absorption spectrum after CDs loading. Pure CD exhibits a distinct characteristic absorption peak near 300 nm, whereas pure $FeV_2S_4$ demonstrates flat linear absorption in this region. When CD is loaded onto the surface of $FeV_2S_4$ to form a heterojunction, the absorption of the composite near 300 nm shifts significantly upward compared to pure $FeV_2S_4$, attributed to the π→π* transition contribution of the carbon core in CD, directly proving the successful loading of CD. Simultaneously, the characteristic absorption peak of CD in the range of 500-600 nm is significantly weakened or even nearly disappears in CD@$FeV_2S_4$, which precisely stems from the formation of tight interface contact and strong electron coupling effect between CD and $FeV_2S_4$. Interface charge transfer and energy level recombination may alter the transition probability of CD's triplet excited state, leading to the suppression of its characteristic absorption in the visible region, thus indirectly confirming the existence of strong non-covalent interface interactions between the two, rather than a simple physical mixture. Furthermore, the zeta potential of positively charged $FeV_2S_4$ shifted from +14.3 mV to a negative value (-17.6 mV) upon CDs loading (Figure 1F). The phenomenon of potential reversal indicates the successful binding of CD with $FeV_2S_4$, along with a change in its surface charge properties. In addition, the hydrodynamic diameters of various materials were measured via dynamic light scattering (DLS). The values for $FeV_2S_4$ and CD@$FeV_2S_4$ were approximately 102.4 nm and 113.7 nm, respectively (Figure 1G).

We utilized XPS to examine the surface chemical properties of CD@$FeV_2S_4$. The main elements such as C, N, O, S, and Fe were detected in the full XPS spectrum of CD@$FeV_2S_4$ (Figure 1H). Among them, Fe primarily exists in the forms of $Fe^{2+}$ and $Fe^{3+}$ (Figure 1I). Compared to the Fe 2*p* spectrum of single-component $FeV_2S_4$, there was no significant shift in peak position or shape in CD@$FeV_2S_4$, indicating that the chemical state of Fe remained stable during the CDs loading process. Similarly, compared to the V 2*p* spectrum of $FeV_2S_4$, V element in CD@$FeV_2S_4$ predominantly existed in the form of $V^{3+}$ (Figure 1J). After CDs loading, a new fitting peak at 167.5 eV emerged in the S 2*p* XPS spectrum of CD@$FeV_2S_4$, which can be assigned to -$SO_3$ on the CDs surface (Figure 1K and S2E). This peak originates from the residual sulfonic acid groups of ICG molecules during CDs preparation, while the inherent S 2*p* peak of $FeV_2S_4$ remains present. Furthermore, the N 1*s* XPS spectrum of CD@$FeV_2S_4$ can be subdivided and fitted into two peaks, corresponding to pyrrolic nitrogen and graphitic nitrogen, respectively (Figure 1L). These peaks aligned with the N 1*s* peaks of single-component CDs (Figure S2C), suggesting that the N-doped structure in CDs was preserved after recombination. In summary, these findings demonstrate that CDs are successfully loaded onto the surface of $FeV_2S_4$, forming a close heterogeneous interface through electrostatic interaction, which lays the material and structural foundation for the subsequent realization of the Z-type charge transfer mechanism.

Following the successful validation of the CD@$FeV_2S_4$ structure, we further systematically evaluated the sonodynamic activity of this composite system. We employed 1,3-diphenylisobenzofuran (DPBF) as a specific probe to monitor ROS to characterize the sonodynamic performance of different materials under US excitation. Firstly, in order to optimize the loading ratio of CD to $FeV_2S_4$, we synthesized three types of heterojunctions with CD to $FeV_2S_4$ mass ratios of 1:1, 2:1, and 4:1, and assessed their sonodynamic activity through DPBF degradation kinetics. As shown in Figure S3, the degradation rate constants were measured at 0.099, 0.155, and 0.137 $min^{-1}$, respectively, with the mass ratio of 2:1 demonstrating the highest sonodynamic activity. Therefore, we selected this mass ratio to prepare CD@$FeV_2S_4$. The experimental results showed that under US irradiation, CD@$FeV_2S_4$ heterojunctions exhibited significantly enhanced ROS generation

ability compared to the single-component CDs (Figure 2A) and $FeV_2S_4$ (Figure 2B). This conclusion was mainly based on the attenuation degree of the characteristic absorption peak of DPBF at 421 nm. In the CD@$FeV_2S_4$ heterojunction system, the attenuation of this absorption peak was more obvious, indicating a higher efficiency of ROS production (Figure 2C). Kinetic tracking demonstrated that the DPBF degradation rate constant for CD@$FeV_2S_4$ reached 0.155 $min^{-1}$, which was 3.30-fold and 2.35-fold greater than those of $FeV_2S_4$ (0.047 $min^{-1}$) and CDs (0.066 $min^{-1}$), respectively (Figure 2D). These outcomes clearly indicated that the Z-scheme heterojunction effectively inhibits the recombination of electron-hole pairs, thereby significantly enhancing the sonodynamic activity of CD@$FeV_2S_4$. To further verify the generation of $^1O_2$ and deeply reveal the generation behavior of ROS, we used electron spin resonance (ESR) technology with 2,2,6,6-tetramethylpiperidine (TEMP) as the $^1O_2$ scavenger to detect the ROS generation ability of CD@$FeV_2S_4$, $FeV_2S_4$, and CDs under US irradiation. As presented in Figure 2E, the CD@$FeV_2S_4$ Z-scheme heterojunction presented a significantly stronger ESR characteristic signal than the single-component $FeV_2S_4$ and CDs, which further confirmed that the introduction of CDs significantly enhanced the sonodynamic performance of the single-component $FeV_2S_4$. Based on the above characterizations, it can be inferred that the carrier transfer mechanism of the Z-scheme heterojunction in CD@$FeV_2S_4$ is the key factor in enhancing the sonodynamic activity.

We explained the sonodynamic enhancement mechanism of the CD@$FeV_2S_4$ heterojunction by detecting the impedance of CD, $FeV_2S_4$ and CD@$FeV_2S_4$. The results showed that the diameter of the semicircle in the Nyquist plot of CD@$FeV_2S_4$ was the smallest (Figure S4). The above finding shows that after CD and $FeV_2S_4$ form a close interface contact, the heterojunction structure substantially reduces the charge transport barrier at the interface, effectively enhancing the interface migration efficiency of carriers. Subsequently, we employed the Tauc plot method to determine that the band gaps of CD and $FeV_2S_4$ were 1.72 eV and 2.59 eV, respectively (Figure 2F, G). Furthermore, by combining XPS-valence band (VB) analysis, the VB positions of CD and $FeV_2S_4$ were found to be 1.68 eV (Figure 2H) and 1.39 eV (Figure 2I), respectively. According to these data, we constructed a schematic diagram of the band structure of the

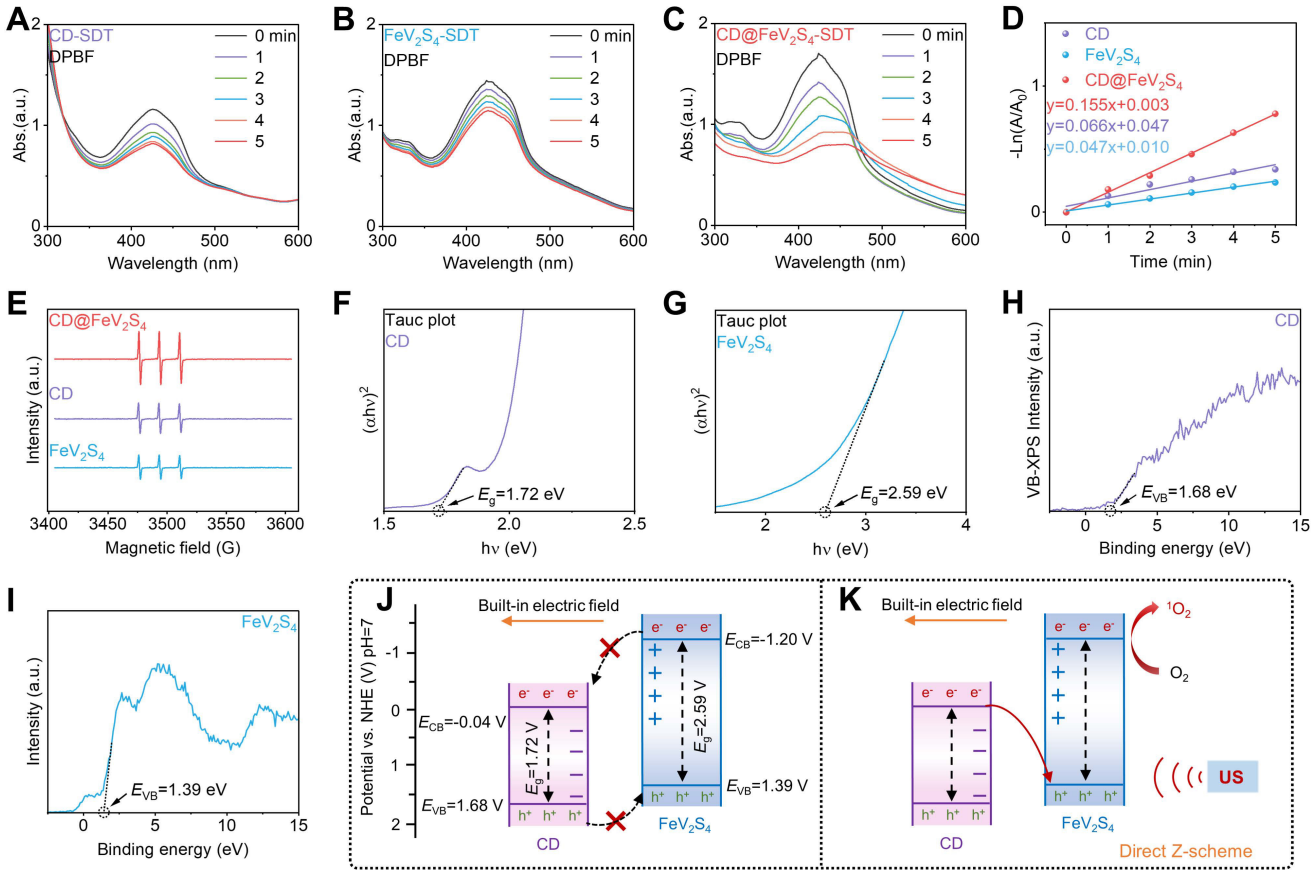



**Figure 2.** (A-D) Evaluation of the SDT performance of CDs, $FeV_2S_4$, and CD@$FeV_2S_4$. (E) ESR measurements of CDs, $FeV_2S_4$, and CD@$FeV_2S_4$ under US irradiation. (F-I) The band gap and valence band of CD and $FeV_2S_4$ were detected through Tauc plot and XPS. (J, K) A schematic diagram shows the energy band diagram of CD@$FeV_2S_4$.

$CD@FeV_2S_4$ heterojunction (Figure 2J). According to the band alignment, if only the energy level positions are considered, there is a thermodynamic possibility of recombination between the conduction band (CB) electrons of CDs and the VB holes of $FeV_2S_4$. However, the built-in electric field between CD and $FeV_2S_4$ affects the direction of charge transfer. Because of the distinct surface charges, an internal electric field pointing from $FeV_2S_4$ to CDs is formed at the interface of the $CD@FeV_2S_4$ heterojunction. Under the influence of this internal electric field, electrons will not spontaneously transfer from the positively charged $FeV_2S_4$ to CDs with negatively charged. Instead, the construction of the internal electric field in the heterojunction promotes the transfer of electrons from the conduction band of CDs to the valence band of $FeV_2S_4$, where they recombine with the holes, thereby retaining carriers with stronger redox capabilities in the two components, namely, the electrons in the CB of $FeV_2S_4$ and the holes in the VB of CDs. This charge transfer path clearly confirms the formation of a Z-scheme heterojunction in the $CD@FeV_2S_4$ composite (Figure 2K). This directional charge transfer at the heterogeneous interface significantly extends the lifetime of charge carriers and effectively suppresses the recombination between electrons and holes, thereby providing a higher concentration of active species for subsequent surface sonocatalytic reactions. From a thermodynamic perspective, the conduction band potential of $FeV_2S_4$ is approximately -1.20 V, which is much more negative than the potential of the $O_2/O_2^-$ redox couple (-0.33 V vs. NHE), which is conducive to the generation of $^1O_2$. Overall, the $CD@FeV_2S_4$ Z-scheme heterojunction achieves a significant enhancement of sonodynamic activity through the synergistic regulation of the band structure and interfacial charge transfer.

Nanocatalytic therapy (NCT) is an emerging tumor treatment strategy that utilizes nanozymes with multiple enzyme-mimic activities to regulate TME and generate ROS. Among the multiple enzyme-mimic activities, POD-like activity can effectively catalyze the excessive $H_2O_2$ in the TME and generate cytotoxic hydroxyl radicals, thereby causing irreversible oxidative damage to tumor cells. Compared with traditional radiotherapy and chemotherapy, NCT has garnered significant attention in recent years due to its advantages, including high tumor selectivity, minimal side effects, and the elimination of the need for external energy input. Given the abundant $Fe^{2+}$ ions in the $CD@FeV_2S_4$ Z-scheme heterojunction, it has the potential to catalyze Fenton-like reactions. 3,3',5,5'-tetramethylbenzidine (TMB) was used as a chromogenic probe to systematically evaluate the POD-like activity of the $CD@FeV_2S_4$ Z-scheme heterojunction. TMB can be oxidized to a blue oxide in the presence of •OH, and the change in its characteristic absorbance at 652 nm can quantitatively reflect the generation level of •OH. The experimental results showed that under weakly acidic conditions (pH 6.0), the absorbance of ox-TMB at 652 nm significantly increased with the increase of $H_2O_2$ concentration for both $CD@FeV_2S_4$ and $FeV_2S_4$ (Figure 3A, B), indicating that both $CD@FeV_2S_4$ and $FeV_2S_4$ could effectively convert $H_2O_2$ into •OH. Kinetic analysis yielded •OH generation rate constants of 1.070 $min^{-1}$ for $CD@FeV_2S_4$ and 0.933 $min^{-1}$ for $FeV_2S_4$ (Figure 3D), Z-scheme structure mildly augmented the Fenton-like efficiency. This effect likely due to the optimization of the electronic structure at the heterojunction interface, thereby accelerating the catalytic decomposition of $H_2O_2$. In contrast, the CDs could not induce any •OH production from $H_2O_2$ (Figure 3C), indicating that CDs do not have POD-like activity, and its role in the composite material is more focused on sonodynamic function and interface charge regulation. The pH value of the TME is usually between 6.0 and 6.8, which is weakly acidic compared to normal tissues (pH 7.4), providing a selective window for pH-responsive treatment. To explore the activity changes of the material under different pH conditions, we further investigated the POD-like performance of the material when the pH was raised to 6.5. The results showed that the •OH generation rates of both $CD@FeV_2S_4$ (Figure 3E) and $FeV_2S_4$ (Figure 3F) decreased, but still maintained a certain catalytic activity (Figure 3H), indicating that both materials could exert POD-like effects within the typical pH range of the TME. Under the same conditions, the CDs still did not show POD-like activity (Figure 3G), further confirming the core role of the $FeV_2S_4$ component in the POD-like reaction. Notably, in a simulated physiological environment with pH 7.4, no obvious •OH generation was detected for either $CD@FeV_2S_4$, $FeV_2S_4$, or CDs (Figure S5). This pH-dependent behavior is of great significance, as the POD-like activity of the material is effectively suppressed in the neutral environment of normal tissues, thereby reducing the risk of non-specific damage to normal cells, while in the weakly acidic TME, its POD-like activity is fully exerted to achieve selective killing of tumor tissues. This endogenous selectivity significantly enhances the biocompatibility of $CD@FeV_2S_4$. To further verify the generation of •OH, we employed ESR spectroscopy with 5,5-dimethyl-1-pyrroline-N-oxide (DMPO) as a specific scavenger for •OH. The ESR results indicated that both $CD@FeV_2S_4$ and $FeV_2S_4$ exhibited typical •OH characteristic signals in the presence of $H_2O_2$ under pH 6.0 (Figure 3I), and the signal intensities were highly

consistent with the results of the TMB colorimetric experiment, further confirming the POD-like reactivity of the CD@$FeV_2S_4$ and $FeV_2S_4$.

In addition to its direct ability to induce oxidative damage, the reduced GSH in the TME is also a key factor affecting the efficacy of ROS-based tumor therapies. As the most abundant endogenous antioxidant in cells, GSH is usually highly expressed in tumor cells, with its content reaching several times or even tens of times that of normal cells. The high concentration of GSH can effectively scavenge exogenous ROS, thereby protecting tumor cells from oxidative stress damage. This mechanism constitutes a major drug resistance barrier for SDT and other ROS-dependent therapeutic strategies. Therefore, we examined the GSH-ox-like performance of CD@$FeV_2S_4$ utilizing DTNB, a probe that yields a peak at 412 nm upon reacting with GSH. As incubation time progressed, the 412 nm absorbance steadily decreased in solutions containing either CD@$FeV_2S_4$ (Figure 3J) and $FeV_2S_4$ (Figure 3L) solutions significantly decreased, indicating that GSH was effectively consumed. This is because $Fe^{3+}$ in CD@$FeV_2S_4$ can undergo a redox reaction with GSH, reducing $Fe^{3+}$ to $Fe^{2+}$ and oxidizing GSH to oxidized glutathione (GSSG), thereby achieving the clearance of GSH. After 12 hours of co-incubation, CD@$FeV_2S_4$ and $FeV_2S_4$ almost completely consumed the GSH in the system (Figure 3K, M). In contrast, CDs did not show GSH-ox-like ability under the same conditions (Figure S6). Notably, the GSH-ox-like ability of CD@$FeV_2S_4$ was comparable to that of $FeV_2S_4$, indicating that the $FeV_2S_4$ component played a dominant role in this process.

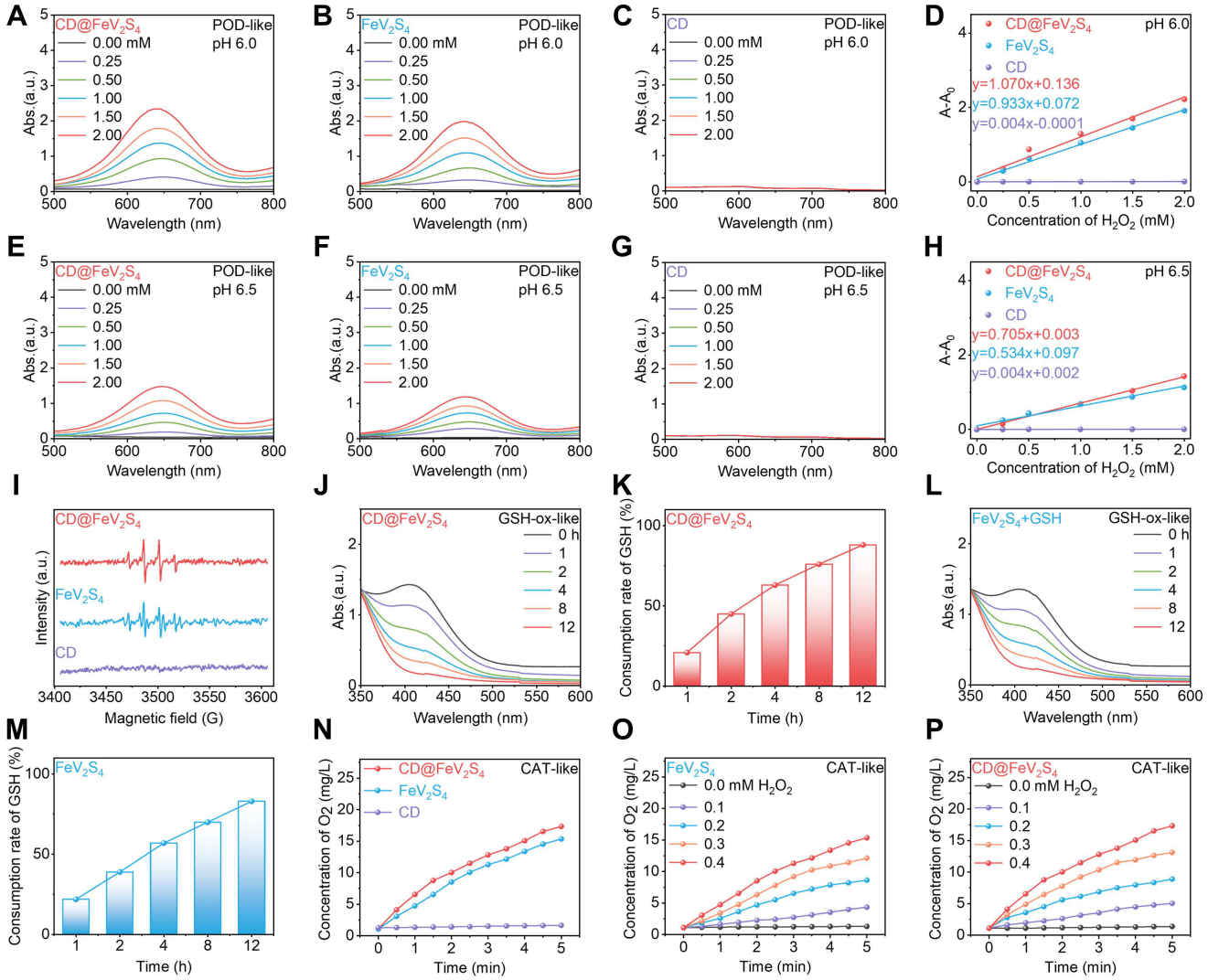



**Figure 3.** (A-H) Measurements of the POD-like activity of CD@$FeV_2S_4$, $FeV_2S_4$, and CDs under pH 6.0 and 6.5. (I) ESR measurements for •OH of CD@$FeV_2S_4$, $FeV_2S_4$, and CDs under pH 6.0. (J-M) Measurements of the GSH-ox-like activity of $FeV_2S_4$ and CD@$FeV_2S_4$. (N) Measurements of the CAT-like activity of CD@$FeV_2S_4$, $FeV_2S_4$, and CDs. (O, P) Measurements of the CAT-like activity of CD@$FeV_2S_4$ and $FeV_2S_4$ at different concentration of $H_2O_2$.

Oxygen ($O_2$) serves as one of the key substrates in SDT and plays a crucial role in tumor treatment. During the US excitation process, oxygen accept energy transfer from sonosensitizers and are excited to $^1O_2$. Therefore, the local oxygen concentration directly determines the efficiency of ROS generation in the SDT process. However, a notable feature of the TME is hypoxia, which is caused by the rapid proliferation of tumor tissues leading to increased oxygen consumption and insufficient oxygen supply due to abnormal vascular structures. In recent years, certain metal-based nanozymes possess CAT-like abilities, breaking down the abundant tumor $H_2O_2$ into $O_2$ to relieve hypoxia *in situ*. Based on this situation, we measured the CAT-like functionality of CD@$FeV_2S_4$ using an oxygen meter to track real-time $O_2$ evolution. The findings showed that under conditions where $H_2O_2$ was present, both CD@$FeV_2S_4$ and $FeV_2S_4$ exhibited significant oxygen generation capabilities, and their oxygen generation ability were nearly equal (Figure 3N), indicating that the $FeV_2S_4$ component was the main contributor to the oxygen generation function. In contrast, no obvious oxygen generation activity was detected for the CDs. We further mixed CD@$FeV_2S_4$ with $H_2O_2$ at different concentration gradients to evaluate its CAT-like activity, the total amount of oxygen generated within 5 minutes was measured. As shown in Figure 3O, P, the oxygen yield gradually increased with the increase in $H_2O_2$ concentration, showing a typical concentration dependent behavior. This property enables CD@$FeV_2S_4$ to fully utilize the overexpressed $H_2O_2$ in the TME, continuously catalyze its decomposition to generate $O_2$, and effectively alleviate the hypoxic state of tumors. In summary, the CD@$FeV_2S_4$ Z-scheme heterojunction demonstrates excellent TME response properties. On the one hand, it can make full use of the excessive $H_2O_2$ in the TME to produce •OH with strong cytotoxicity, thereby achieving highly efficient NCT. On the other hand, it can also alleviate the hypoxia problem in tumors by catalyzing $H_2O_2$ to produce $O_2$, thereby significantly enhancing the activity of SDT. In addition, its excellent GSH consumption performance further prevents the consumption of ROS, thereby amplifying intracellular oxidative stress. These characteristics collectively endow CD@$FeV_2S_4$ with great potential in tumor treatment.

To systematically explore the potential application of the CD@$FeV_2S_4$ Z-scheme heterojunction in tumor therapy. Firstly, we evaluated the synergistic antitumor effect of SDT-NCT on CD@$FeV_2S_4$. The NIH-3T3 and the CT26 cell were selected as the normal cell model and the tumor cell model to assess the biocompatibility of CD@$FeV_2S_4$ respectively. Firstly, the biocompatibility of CD@$FeV_2S_4$, $FeV_2S_4$, and CDs were systematically tested using the MTT method. The results showed that under different concentration conditions, after co-incubation with NIH-3T3 cells, the cell survival rates of the three materials were all maintained at a high level (> 90%) (Figure 4A, B and S7A), indicating that none of the three materials exhibited obvious cytotoxicity to normal cells and demonstrated good biocompatibility, laying a safety foundation for subsequent antitumor applications. Furthermore, we investigated the cytotoxicity of CD@$FeV_2S_4$ and $FeV_2S_4$ to CT26 cells under a single NCT treatment mode. The experimental results indicated that when CT26 cells were exposed to varying concentrations of CD@$FeV_2S_4$ or $FeV_2S_4$ alone, the cytotoxicity induced by both materials was relatively limited. Even after elevating the material concentration to 100 μg/mL, the cell survival rates of the $FeV_2S_4$ and CD@$FeV_2S_4$ treatment groups were still as high as 70.6% and 61.1%, respectively (Figure 4C, D), suggesting that a single NCT treatment strategy was insufficient to effectively eliminate tumor cells. Additionally, single CD showed no significant growth inhibitory effect on CT26 cells (Figure S7B), further confirming that CD itself did not possess significant antitumor activity, and its main role in the composite system was to synergistically enhance the SDT efficacy. To evaluate the synergistic effect of CD@$FeV_2S_4$ in SDT and NCT combined therapy, US irradiation was introduced during the treatment process, and the survival of CT26 cells under different treatment was compared. The results showed that under US irradiation, the cell survival rates of the $FeV_2S_4$, CDs, and CD@$FeV_2S_4$ treatment groups all decreased significantly. Specifically, after $FeV_2S_4$ + US or CD@$FeV_2S_4$ + US treatment, the cell survival rate dropped to approximately 38.3% (Figure 4C) and 9.5% (Figure 4D), respectively. These findings clearly indicate that constructing a Z-scheme heterojunction significantly enhance the tumor-killing ability of CD@$FeV_2S_4$, and the introduction of US irradiation further amplified the synergistic therapeutic effect.

To visually demonstrate the impact of different treatment methods on the survival status of cells, we conducted a live/dead fluorescence staining experiment and compared six treatment groups (Control, US, $FeV_2S_4$, CD@$FeV_2S_4$, $FeV_2S_4$ + US, CD@$FeV_2S_4$ + US). As shown in Figure 4E, within CD@$FeV_2S_4$ + US group, the signal of red fluorescence (dead cells) was significantly increased, whereas the signal of green fluorescence (live cells) significantly decreased, clearly indicating that this combined treatment strategy exhibited the strongest killing efficacy against tumor cells. In contrast, in the other groups without US irradiation, the green fluorescence

still dominated, further confirming the limitations of single treatment methods in tumor cell clearance. ROS are key effector molecules in SDT and NCT therapy, and their generation level directly determines the therapeutic efficiency. Therefore, we employed the DCFH-DA probe to quantify the intracellular accumulation of ROS. As shown in Figure 4F, neither the control nor US alone groups displayed notable green fluorescence. In the $FeV_2S_4$ and $CD@FeV_2S_4$ treatment groups, weak green fluorescence was observed, mainly due to the ROS species such as •OH generated by the Fenton-like catalytic reaction mediated by $FeV_2S_4$.

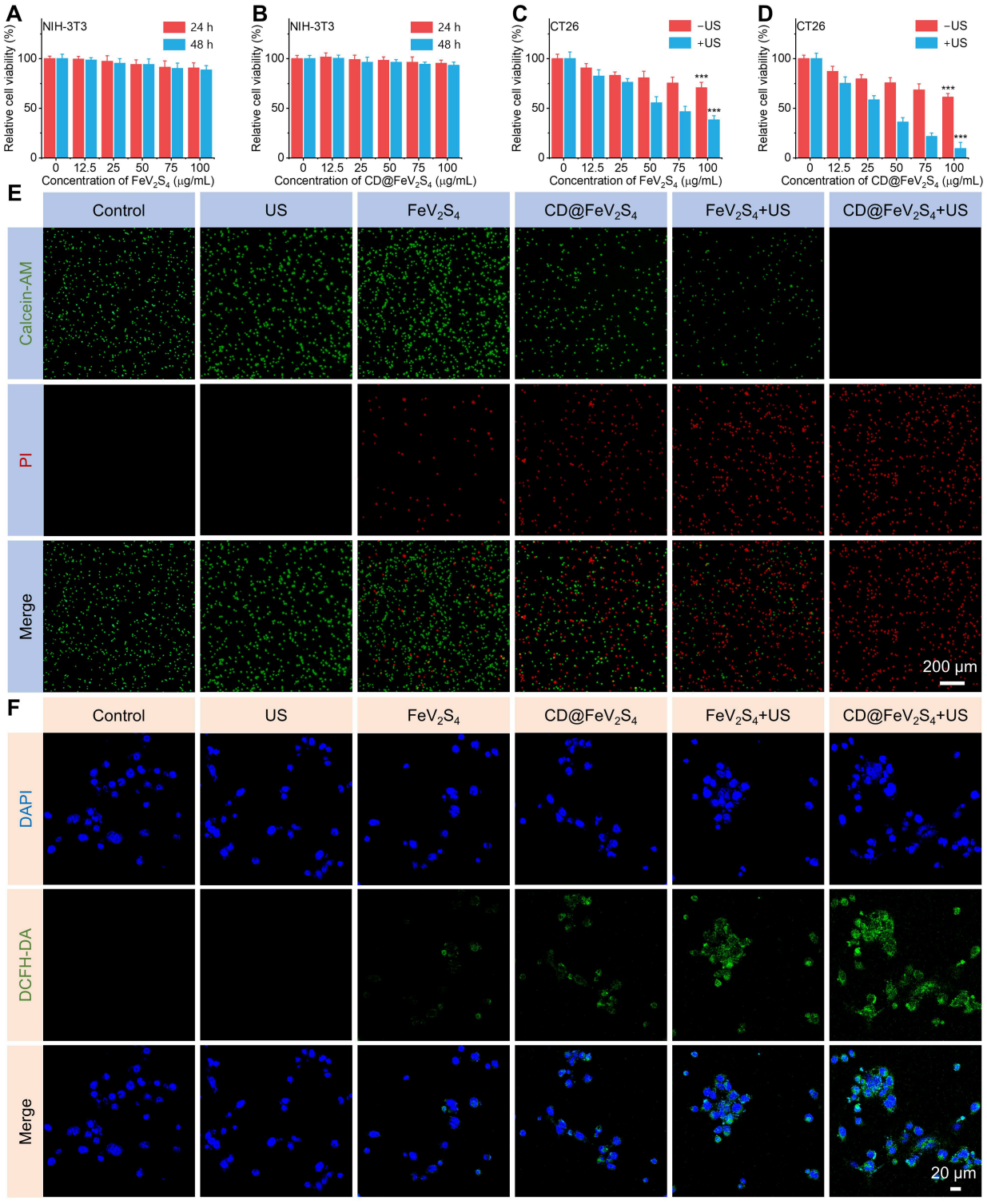



**Figure 4.** (A, B) Cytotoxicity assessment of $FeV_2S_4$ and $CD@FeV_2S_4$ towards NIH-3T3 cells. (C, D) Cytotoxicity assessment of $FeV_2S_4$ and $CD@FeV_2S_4$ towards CT26 cells. (E, F) Live/dead and ROS staining assay of CT26 cells after different treatments. Data are presented as the mean ± SD. (n = 6). ***p < 0.001.

Notably, under US irradiation conditions, compared to the $FeV_2S_4$ group, the $CD@FeV_2S_4$ Z-scheme heterojunction formed after loading CDs exhibits a stronger green fluorescence signal by amplifying the generation of ROS. This enhancement effect can be attributed to the efficient carrier separation and migration behavior at the heterojunction interface, allowing the electrons generated during the sonodynamic process to more effectively participate in the ROS generation reaction.

For the validation of ROS dependency, we added the ROS scavenger N-acetylcysteine (NAC) to the $CD@FeV_2S_4$ + US treatment group, the experimental results revealed that upon the additional administration of NAC, the green fluorescence signal significantly diminished (Figure S8). This result confirms that the ROS production triggered by $CD@FeV_2S_4$ + US serves as the upstream trigger event for subsequent biological effects, and this effect can be effectively reversed by NAC.

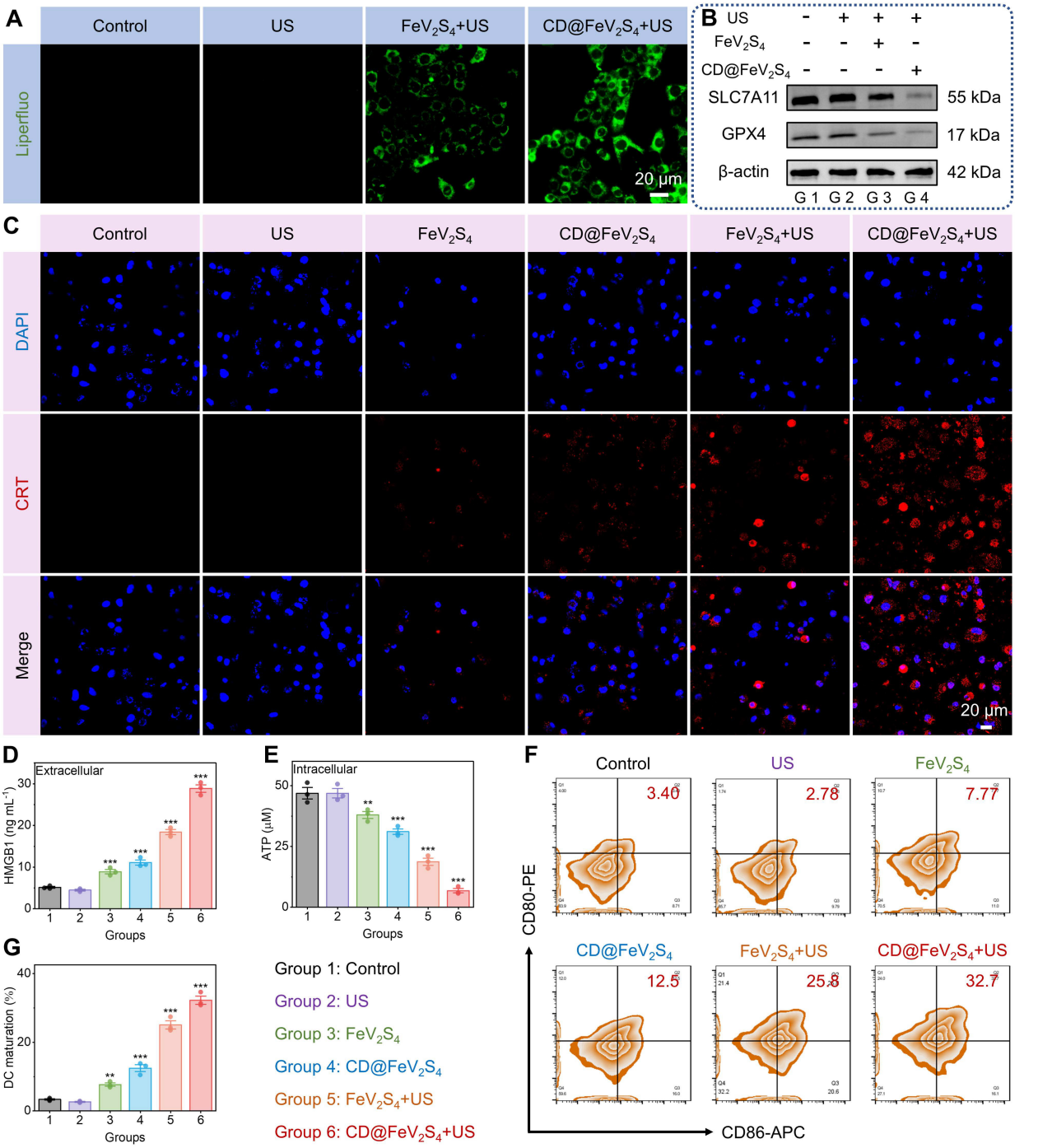



**Figure 5.** (A) Evaluation of intracellular lipid peroxidation (LPO) in CT26 cells subjected to indicated treatments. (B) Protein levels of GPX4 and SLC7A11 in different groups. (C-E) Measurements of CRT, HMGB1 and ATP levels in CT26 cells in different groups. (F, G) Flow cytometric analysis of CD80 and CD86 on DCs exposed to different treatments. Data are presented as the mean ± SD. (n = 3). **p < 0.01 and ***p < 0.001.

Excessive ROS accumulation can induce mitochondrial damage and subsequently trigger apoptotic cascades. The JC-1 probe is used to detect mitochondrial damage after different treatments. When the membrane potential collapses, this dye transitions from red aggregates to green monomers. The shift from red to green fluorescence can reflect the degree of mitochondrial functional damage. Confocal laser scanning microscopy images revealed that the CD@$FeV_2S_4$ + US group presented the most significant green fluorescence signal and the weakest red fluorescence signal (Figure S9), suggesting that this treatment method caused the most severe mitochondrial functional damage. This result was highly consistent with the ROS detection results, indicating that the ROS efficiently generated by the Z-type heterojunction under US excitation can effectively target and damage mitochondria, disrupt the energy metabolism center, and thereby amplify the cell death signal. Additionally, we employed flow cytometry to quantitatively assess the apoptosis levels of cells across different groups. The research results indicate that, compared with the control group, CT26 cells treated with CD@$FeV_2S_4$ + US underwent significant apoptosis, with a total apoptosis rate of 72.4%. (Figure S10). further verifying the high antitumor efficacy of CD@$FeV_2S_4$ in SDT-NCT synergistic therapy. This apoptosis rate was much higher than that of the $FeV_2S_4$ + US group and the control group, fully demonstrating the synergistic effect of the heterojunction structure in the synergistic treatment. The above *in vitro* experimental data consistently indicate that CD@$FeV_2S_4$ has excellent antitumor performance. Its good biocompatibility, efficient ROS generation ability, significant induction of mitochondrial damage, and strong triggering of cell apoptosis collectively form the basis of its SDT-NCT synergistic therapy.

The excellent SDT activity of CD@$FeV_2S_4$ enables it to continuously produce a substantial quantity of ROS under irradiation of US. These excessive ROS can directly attack the polyunsaturated fatty acids (PUFAs) abundant in cell membrane, thereby initiating a lipid peroxidation cascade reaction and causing oxidative damage to the membrane structure [52, 55]. The liperfluo fluorescent probe was used to specifically detect the level of lipid peroxides. As depicted in Figure 5A, compared with the control group, the $FeV_2S_4$ + US group can already induce lipid peroxidation, indicating that $FeV_2S_4$ has certain SDT activity under US excitation. For comparison, the CD@$FeV_2S_4$ + US group formed after constructing a Z-type heterojunction has a further enhanced lipid peroxidation signal, and its fluorescence intensity was notably higher than that observed in the $FeV_2S_4$ + US group. What's more, we also detected the expression of malondialdehyde (MDA) and 4-hydroxynonenal (4-HNE), which are key lipid peroxidation products in the ferroptosis process. The experimental results indicated that, in comparison to the control and the US group, the MDA content was upregulated to a certain extent in the $FeV_2S_4$ and the CD@$FeV_2S_4$ group. Furthermore, MDA levels increased significantly in the $FeV_2S_4$ + US group, with the CD@$FeV_2S_4$ + US group exhibiting the highest MDA content compared to other groups (Figure S11A). Consistent with these findings, we simultaneously detected another typical ferroptosis marker, 4-hydroxynonenal (4-HNE), whose expression trend mirrored that of MDA, with the highest positive signal also detected in the CD@$FeV_2S_4$ + US group (Figure S11B). These results confirm that the Z-type charge separation mechanism effectively amplifies the SDT activity, promotes the efficient separation of electrons and holes, and thereby increases the ROS production rate and lipid peroxidation efficiency.

Recently, existing studies have confirmed that ROS can synergistically inhibit the key negative regulatory factors of ferroptosis through two pathways, thereby tightly coupling oxidative stress with the ferroptosis process [56-58]. On the one hand, ROS can activate transcription factors such as p53, down-regulating the expression of SLC7A11 (cystine/glutamate antiporter) at the transcriptional level. On the other hand, ROS can also promote the degradation of SLC7A11 protein through the ubiquitin-proteasome pathway. The decrease in SLC7A11 expression leads to the obstruction of extracellular cystine uptake, resulting in a lack of raw materials for GSH synthesis, ultimately causing the inactivation of glutathione peroxidase 4 (GPX4) due to the lack of cofactors. GPX4 is the only key enzyme in the cell capable of eliminating lipid peroxides, and its loss of function eliminates the clearance ability for lipid peroxides, allowing the already initiated lipid peroxidation reaction to uncontrollably expand and ultimately trigger ferroptosis irreversibly. The results of western blotting indicate that CD@$FeV_2S_4$ + US treatment significantly down-regulated the protein expression levels of SLC7A11 and GPX4 in tumor cells (Figure 5B and S12), accompanied by a significant decrease in intracellular GSH content (Figure S13), confirming the activation of the ferroptosis pathway at the molecular level. To further confirm the role of ferroptosis in this treatment strategy, we conducted inhibitor rescue experiments, after adding ferroptosis-specific inhibitor Ferrostatin-1 to the CD@$FeV_2S_4$ + US treatment system, the originally down-regulated protein expression levels of SLC7A11 and GPX4 were significantly restored (Figure S14), and the cell survival rate also rebounded accordingly (Figure S15).

To further exclude interference from other cell death modalities and confirm the specificity of ferroptosis, we introduced the apoptosis inhibitor Z-VAD-FMK and the necrosis inhibitor Nec-1 for intervention experiments. WB analysis revealed that, even when Z-VAD-FMK or Nec-1 was present, the expression levels of GPX4 and SLC7A11 proteins were markedly reduced following treatment with CD@$FeV_2S_4$ + US (Figure S16). This result strongly supports that ferroptosis is one of the core execution mechanisms of CD@$FeV_2S_4$ + US in exerting antitumor effects.

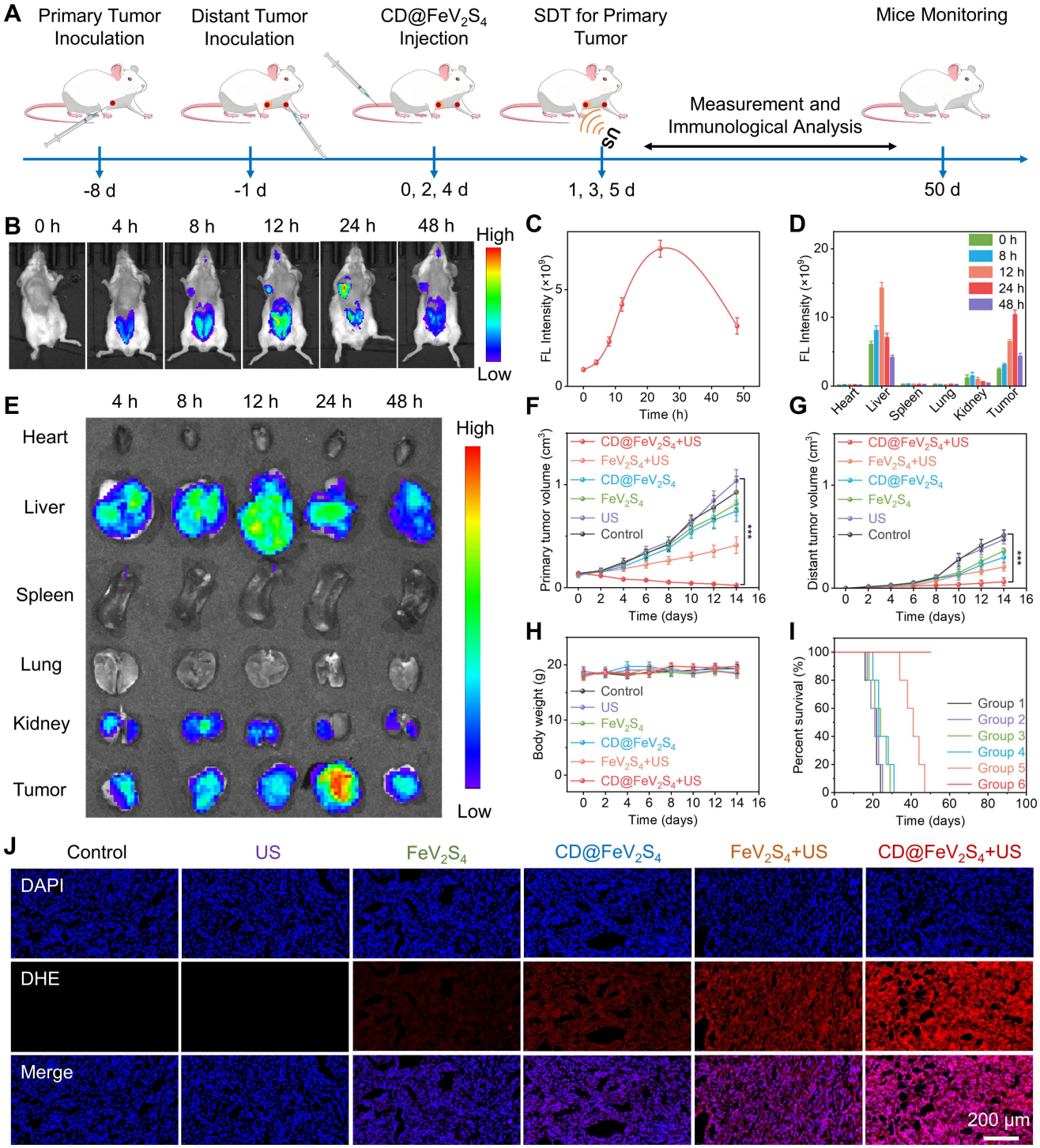



**Figure 6.** (A) A schematic illustration of the *in vivo* antitumor therapy employing the CD@$FeV_2S_4$ Z-scheme heterojunction. (B-E) NIR fluorescence imaging of CT26 tumor-bearing mice following intravenous administration of ICG labeled CD@$FeV_2S_4$. Data are presented as the mean ± SD. (n = 3). (F-J) Measurements of primary and distant tumor volume, body weight, survival of mice and DHE staining in tumor tissues after different treatments. Data are presented as the mean ± SD. (n = 5). ***$p < 0.001$.

Notably, the burst of ROS and ferroptosis process have been confirmed to be able to synergistically induce ICD [47, 59], a type of cell death that capable of activating antitumor immune response [49, 50]. Its typical characteristics include the orderly release and exposure of DAMPs [48], which mainly consist of three aspects. First, ecto-CRT on the cell membrane surface translocates from the intracellular region to the extracellular region, providing a "eat me" signal for phagocytes [60]. Second, HMGB1 in the nucleus is actively secreted to the extracellular space, exerting a pro-inflammatory signaling role [61]. Third, the active release of cytoplasmic ATP to the extracellular space serves as a chemotactic signal for the recruitment of antigen-presenting cells [62]. These DAMPs together constitute the molecular basis for immune activation, promoting the recognition, uptake, and cross-presentation of tumor antigens by DCs [59], and thereby activating tumor-specific T cell responses [49], achieving the transformation from innate immunity to adaptive immunity [50]. Therefore, we systematically verified the ability of CD@$FeV_2S_4$ + US to induce ICD. Immunofluorescence staining showed that the ecto-CRT exposure level on the surface of CT26 cells in the CD@$FeV_2S_4$ + US group was the highest, and the fluorescence signal was significantly stronger than that in other treatment groups (Figure 5C). ELISA quantitative results confirmed that the concentration of HMGB1 in the culture supernatant of this group was significantly higher than that in other groups (Figure 5D), indicating that a large amount of nuclear protein was released to the extracellular space. ATP assay kit analysis further showed that the intracellular ATP level was significantly decreased in the CD@$FeV_2S_4$ + US treatment group (Figure 5E), suggesting that a large amount of ATP was actively secreted to the extracellular space, and this phenomenon is one of the key indicators of ICD occurrence. The consistent increase in the response of these three types of DAMPs fully confirms that CD@$FeV_2S_4$ + US, by synergistically enhancing SDT therapy and ferroptosis, can efficiently trigger a powerful ICD effect. Given that DAMPs are the key initiating signals for the maturation of DCs, we further explored their immune activation effects. We isolated bone marrow cells from BALB/c mice, and under the combined induction of GM-CSF and IL-4, we obtained immature dendritic cells (BMDCs) through *in vitro* culture. Subsequently, using the conditioned culture supernatants of CT26 tumor cells treated with different treatment groups (Control, US, $FeV_2S_4$, CD@$FeV_2S_4$, $FeV_2S_4$ + US, CD@$FeV_2S_4$ + US) as the antigen source were co-incubated with BMDCs to simulate the process of DCs taking up antigens and maturing in the TME. Flow cytometry revealed that CT26 cells treated with CD@$FeV_2S_4$ + US released the highest amount of tumor antigens, thereby inducing the greatest maturation of BMDCs, with the highest expression levels of CD80 and CD86 (Figure 5F, G). This result indicates that the potent ICD induced by CD@$FeV_2S_4$ + US not only can generate abundant DAMPs signals, but also can effectively drive DCs to complete maturation, enabling them to acquire efficient antigen presentation capabilities, laying a key foundation for the subsequent initiation of adaptive immune responses.

To systematically evaluate the anti-tumor efficacy of CD@$FeV_2S_4$ *in vivo*, this study constructed a mouse bilateral homologous tumor model and conducted therapeutic experiments according to the scheme shown in Figure 6A. This model was established by inoculating the same tumor cells symmetrically on both sides of the animal's body, enabling simultaneous monitoring of the inhibitory effect of the material on the primary lesion (tumor irradiated by ultrasound) and the distant untreated lesion, thereby verifying its potential systemic antitumor activity, especially suitable for evaluating the remote effects induced by the treatment strategy. Firstly, we employed ICG to fluorescently label CD@$FeV_2S_4$, aiming to accurately identify the optimal intervention time window for SDT. The *in vivo* accumulation of CD@$FeV_2S_4$ after intravenous injection was monitored using a animal imaging system. The results indicated the strongest fluorescence signal was detected at the tumor site after 24 hours. (Figure 6B-E), confirming that CD@$FeV_2S_4$ can efficiently target and accumulate in tumor tissues through the enhanced the permeability and retention effect (EPR effect). This effect constitutes the fundamental mechanism underlying the passive targeting of nanomaterials in solid tumors, which relies on the incomplete vascular structure and dysfunction of lymphatic drainage in tumor tissues, allowing nanoscale materials to selectively accumulate within the tumor [63]. Based on the above time-space distribution characteristics, the US irradiation time was uniformly set to 24 hours after administration to ensure that the material concentration within the tumor reached its maximum during the treatment, thereby improving the efficiency of SDT and ensuring the consistency of treatment conditions.

Subsequently, the therapeutic effect was assessed by monitoring the volume changes of the primary tumors and the distant tumors. As depicted in Figure 6F, G and S17, the groups that were given $FeV_2S_4$ alone or CD@$FeV_2S_4$ (without US irradiation) had a weak inhibitory effect on tumor growth, suggesting that the efficacy of single NCT was limited. This result aligns with the trend observed in the *in vitro* cell experiments.

However, after introducing US irradiation, the tumor suppression effect was significantly enhanced. Especially in the CD@$FeV_2S_4$ + US group, following three intravenous injections in combination with three ultrasound therapies, the primary tumor's growth was significantly inhibited., and the distant tumors showed a significant decrease trend. It is noted that the distant tumors still exhibited significant inhibition effect under the condition of receiving the same administration but without US irradiation. This phenomenon cannot be solely explained by the direct killing effect of the material, suggesting that US irradiation amplifies the production of ROS and further stimulates the antitumor immune response. In addition, we mechanically mixed CD and $FeV_2S_4$ in the same mass ratio (2:1) as that prepared for CD@$FeV_2S_4$. Subsequently, this physical mixture (CD + $FeV_2S_4$) was employed for the treatment of bilateral tumor-bearing mice under identical administration protocols and US irradiation conditions. The results revealed that the inhibition rate of primary tumor growth in the CD + $FeV_2S_4$ physical mixture combined with US treatment group was merely 42.3% (Figure S18), whereas the CD@$FeV_2S_4$ + US group achieved a remarkable tumor inhibition rate of 97.6% (Figure 6F). This comparative data indicates that a simple physical blending of CD and $FeV_2S_4$ fails to effectively exert the synergistic therapeutic effects. This result substantiates that heterojunction interface engineering, rather than the simple superposition of materials, is the pivotal factor underlying the outstanding antitumor efficacy achieved. Throughout the treatment period, the body weight of mice in all groups remained largely unchanged (Figure 6H), showing no statistically significant difference compared to the control group, indicating that CD@$FeV_2S_4$ has good biocompatibility and low systemic toxicity. Additionally, the mice in the CD@$FeV_2S_4$ + US group survived for over 50 days (Figure 6I), markedly outperforming the other groups. This further confirms that this strategy has both safety and long-term therapeutic potential. Notably, compared to the tumor recurrence and shortened survival period observed in other treatment groups in the later stage of treatment, the mice in the CD@$FeV_2S_4$ + US group maintained a good survival status throughout the observation period, suggesting that this synergistic treatment strategy not only achieves immediate tumor suppression but also helps establish long-term tumor inhibition effects. The aforementioned findings demonstrate that the SDT-NCT synergistic therapeutic system, built upon the Z-type heterojunction CD@$FeV_2S_4$, not only effectively suppresses local tumor progression but also trigger a systemic immune response, ultimately significantly extending the survival duration of tumor-bearing mice, demonstrating its superiority as an *in vivo* antitumor strategy.

Subsequently, we performed a multidimensional histopathological examination on the tumor tissues of mice subjected to various treatments. DHE staining demonstrated that the reactive oxygen species (ROS) levels within the tumors of the CD@$FeV_2S_4$ + US group were markedly elevated compared to those in the other groups (Figures 6J and S19), directly confirming the material's ability to efficiently generate ROS under US exposure. We further demonstrated the antitumor effect of CD@$FeV_2S_4$ + US treatment through histological staining. H&E and TUNEL staining of primary tumor tissue sections showed significant tissue necrosis and widespread apoptosis in tumor tissue after CD@$FeV_2S_4$ + US treatment (Figure S20). The necrotic area occupied the main area of the tumor section, and typical pathological changes such as nuclear shrinkage, fragmentation, and dissolution were observed. The distant tumors also observed the same degree of damage characteristics (Figure S21), indicating that the therapeutic effect could break through local limitations and produce a distant effect. We further conducted Ki67 immunohistochemical staining on tumor tissue sections from each group after treatment to assess the inhibition of tumor cell proliferation. The experimental results showed that the proportion of Ki67-positive cells was higher in the control group and the US-only group, exhibiting a large amount of brownish-yellow positive staining, indicating active tumor cell proliferation. However, in the CD@$FeV_2S_4$ + US group, the Ki67 positive signal was extremely weak, and the proportion of positive cells was significantly reduced, suggesting that this combined treatment almost completely inhibited tumor cell proliferation (Figure S22). In addition, we also conducted WB assay on tumor tissues from mice in each group after treatment to verify whether CD@$FeV_2S_4$ + US can also induce ferroptosis *in vivo*. The results indicated that, in alignment with the outcomes of *in vitro* cell experiments, after treatment with CD@$FeV_2S_4$ + US, the protein expression levels of GPX4 and SLC7A11 were markedly reduced in tumor tissues (Figure S23), while there were no significant changes in the expression of these two proteins in the control group and the US-only group, indicating that CD@$FeV_2S_4$-mediated combination therapy can effectively trigger ferroptosis *in vivo*. These results confirmed that this treatment strategy can activate the systemic immune response of the body and achieve effective inhibition of distant untreated tumors.

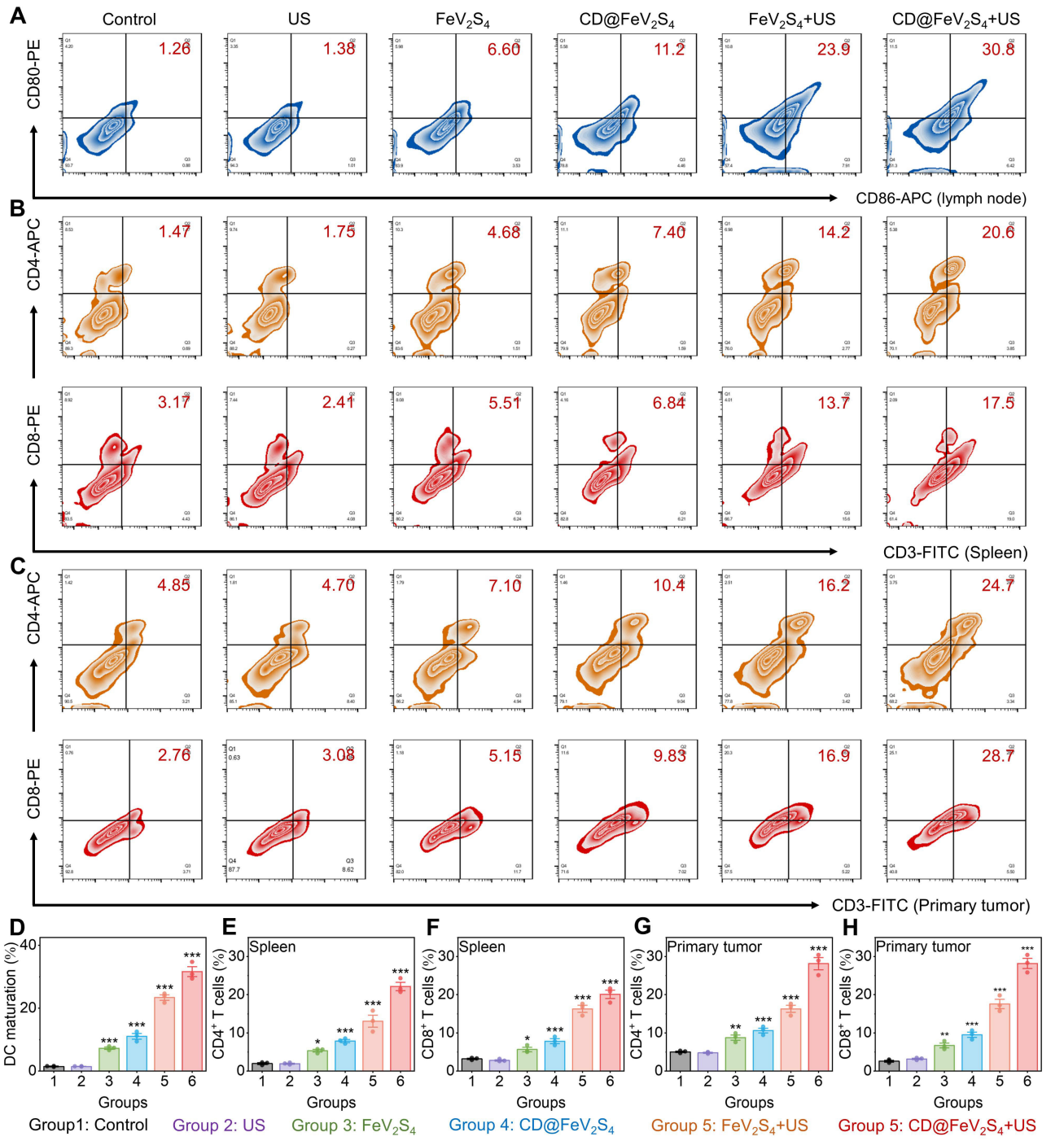



**Figure 7.** (A, D) Assessment of DC maturation level in lymph nodes at different groups. (B, E, F) Evaluation of splenic T cell activation level in different groups. (C, G, H) Analysis of T cell activation within the primary tumors in different groups. Data are presented as the mean ± SD. (n = 3). *p < 0.05, **p < 0.01, and ***p < 0.001.

We further explored the potential of this treatment strategy in activating the antitumor immune response *in vivo*. The effective activation of the immune system is a crucial step in achieving long-term control and distant suppression of tumors. Therefore, clarifying the regulatory role of this treatment system on the immune response is of great significance for a comprehensive assessment of its therapeutic value. On this basis, We first evaluated the levels of pro-inflammatory cytokines in mice, including tumor necrosis factor-α (TNF-α), interferon-γ (IFN-γ), and interleukin-12 (IL-12), using the ELISA method. As shown in Figure S24, compared to other groups, the levels of TNF-α, IL-12, and IFN-γ were significantly elevated in the CD@$FeV_2S_4$ + US group. These findings suggest that SDT mediated by CD@$FeV_2S_4$ can trigger an *in vivo* immune response through the release of tumor-associated antigens, ultimately leading to ICD and further inducing DC maturation. We then evaluated the induction level of ICD by detecting the

release of HMGB1 and ATP in tumor tissues. These two typical DAMPs are released extracellularly when tumor cells undergo ICD and are key signals for initiating the antitumor immune response [64]. As illustrated in Figure S25, compared with using CD@$FeV_2S_4$ alone, after combined treatment with CD@$FeV_2S_4$ and US irradiation, the release of HMGB1 and ATP in tumor tissues increased by 2.33 times and 2.21 times, respectively. In addition, compared with the control group, the release of HMGB1 and ATP in CD@$FeV_2S_4$ + US group increased by 6.69 times and 5.01 times, respectively. These results indicate that the introduction of SDT significantly amplified the generation of ROS, thereby inducing more tumor cells to undergo ICD. The effective release of these DAMPs laid a key foundation for further promoting the maturation of DCs and the activation of subsequent antitumor T cell responses.

To test this hypothesis, we harvested tumor-draining lymph nodes (TDLN), spleen, and tumor tissue samples from each group of mice, and conducted a systematic analysis of different immune cell populations using flow cytometry. The TDLNs are the key sites where antigen-presenting cells interact with T cells, and the maturation status of DCs within them directly determines the intensity and quality of the subsequent immune response [65]. As shown in Figure 7A, D, in TDLNs, the proportion of mature DCs significantly increased from 1.26% in the control group to 11.2% in the CD@$FeV_2S_4$ group, and even reached 30.8% in the CD@$FeV_2S_4$ + US group, indicating a highly significant improvement in the maturity of DCs. This trend suggests that the ICD induced by CD@$FeV_2S_4$-mediated combination therapy can effectively promote the activation and maturation of DCs. As a pivotal link in the immune response, mature dendritic cells (DCs) can efficiently present tumor antigens to T lymphocytes, thereby providing the necessary signals for the subsequent proliferation, activation, and differentiation of these cells into

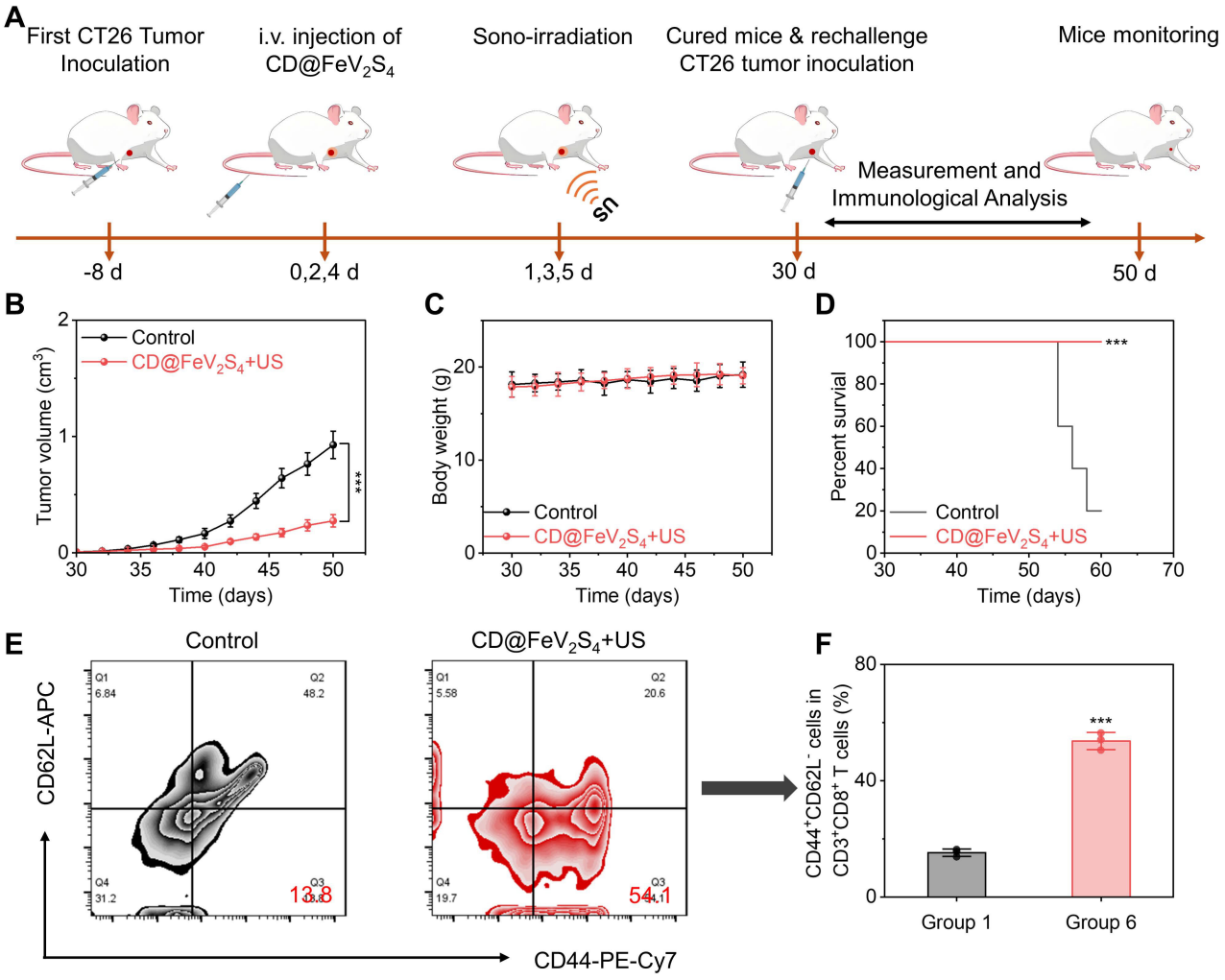



**Figure 8.** (A) Diagram showing the *in vivo* rechallenge antitumor treatment of CD@$FeV_2S_4$ Z-type heterojunction. (B) Measurement of tumor volume in different groups. (C) Measurement of body weight in different groups. (D) Measurement of survival of mice in different groups. (E, F) Measurement of $CD8^+$ memory T cells ($CD3^+CD8^+CD44^+CD62L^-$) in spleen of mice with flow cytometric. Data are presented as the mean ± SD. (n = 5). ***$p < 0.001$.

effector T cells, ultimately exerting antitumor immune killing effects. Subsequently, we evaluated the changes in T lymphocytes in spleens. As the largest peripheral immune organ of the body, is an important window reflecting the level of systemic immune response [66]. After CD@$FeV_2S_4$ + US treatment, the percentages of $CD4^+CD3^+$ T cells and $CD8^+CD3^+$ T cells in the spleens significantly increased from 1.47% and 3.17% in the control group to 20.6% and 17.5% (Figure 7B, E, F), indicating that this treatment strategy significantly enhanced the activation and proliferation ability of T lymphocytes in systemic immune organs. Among them, $CD8^+$ T cells, as the main cytotoxic T lymphocytes, the significant increase in their number directly relates to the intensity of the antitumor effect, while $CD4^+$ T cells play an indispensable role in the regulation of the immune response by maintaining the function of $CD8^+$ T cells and forming immune memory [67]. The synergistic enhancement of these two T cell subsets provides a solid foundation for the establishment of a durable and efficient antitumor immune response.

In addition to the changes in T cells in the spleen, we also focused on the infiltration of T cells in tumor tissues. The number and functional state of tumor-infiltrating lymphocytes are important indicators for measuring the intensity of antitumor immune response and directly determine the final effect of tumor immunotherapy [68]. The results showed that compared with other groups, in both primary tumors (Figure 7C, G, H) and distant tumors (Figure S26), the expression levels of $CD8^+CD3^+$ T cells and $CD4^+CD3^+$ T cells in the CD@$FeV_2S_4$ + US treatment group were significantly increased. It is noteworthy that significant infiltration and activation of T cells were also observed in distant tumors, further indicating that this treatment strategy can activate systemic immunity. The enrichment of T cells was observed in distant tumors without US irradiation, further confirming that the immune response induced by this treatment system has systemic characteristics and can break through the limitations of local treatment to achieve systemic immune surveillance and tumor suppression. These results indicate that CD@$FeV_2S_4$ combined with US treatment not only can effectively activate the immune response in the local TME but also can achieve the inhibitory effect on distant untreated tumors through systemic immune regulation, demonstrating good antitumor immunity and remote effects. The cascade amplification of these immune events constitutes the immunological basis for this treatment strategy to achieve dual inhibition of local and distant tumors.

To further validate the immune memory triggered by the CD@$FeV_2S_4$-mediated combined therapy, we constructed a tumor rechallenge model. On day -8, CT26 cells were implanted into the right armpit of the mice. CD@$FeV_2S_4$ was administered on days 0, 2, and 4, followed by ultrasound irradiation (50 kHz, 3.0 W/$cm^2$, with a 50% duty cycle) on days 1, 3, and 5. On day 30, CT26 cells were implanted into the left armpit of mice that had achieved complete tumor regression, while another five healthy mice were also implanted with tumor cells to serve as controls (Figure 8A). Compared to the control group, the growth of re-challenged tumors in mice treated with CD@$FeV_2S_4$ + US was significantly inhibited (Figure 8B). Moreover, throughout the observation period, there was no significant change in the body weight of mice in both the CD@$FeV_2S_4$ + US group and the control group (Figure 8C), and their survival rate was notably extended (Figure 8D). These findings CD@$FeV_2S_4$ + US treatment can effectively activate the immune memory effect to prevent tumor recurrence. Next, we further detected the activation of memory T cells through flow cytometry. As shown in Figures 8E and 8F, the level in the CD@$FeV_2S_4$ + US group was 3.92 times higher than that in the control group (13.8%). These findings convincingly show that CD@$FeV_2S_4$ + US therapy can induce a durable immune memory response and significantly inhibit tumor recurrence.

Finally, comprehensive biosafety evaluations were conducted to validate the clinical viability of CD@$FeV_2S_4$. H&E staining of the main organs in different treatments revealed no obvious damage compared to the control group (Figure S27). Additionally, blood biochemical analysis (Figure S28) and hematological indices (Figure S29) remained firmly within standard physiological thresholds, denoting pristine blood compatibility. Biodistribution tracking indicated that the nano-system primarily accumulated in the liver and spleen at the 24-hour mark due to reticuloendothelial capture, but the vanadium signal faded almost entirely by day 14 (Figure S30). Analysis of the excretory pathways showed a steady decline of the V signal in both feces and urine down to trace amounts (Figure S31), confirming that the composite is safely cleared from the host via hepatic and renal routes. These exhaustive toxicity assessments firmly establish the superior biocompatibility and biosafety of the CD@$FeV_2S_4$ therapeutic platform.

## Conclusion

In summary, we successfully designed and constructed a novel Z-scheme heterojunction sonozyme, CD@$FeV_2S_4$, to achieve cascade amplification of ROS production and activate systemic anti-tumor immune response. From the perspective of material design, $FeV_2S_4$, as a binary metal sulfide, has

not been previously reported for use in the SDT field, nor has it been studied in combination with CDs to construct a heterojunction sonodynamic system. Therefore, the material design of the CD@$FeV_2S_4$ Z-scheme heterojunction is original. The combination of bimetallic sulfide $FeV_2S_4$ nanozymes and CD sonosensitizers endowed the Z-scheme heterojunctions with excellent multienzyme-mimic activities (POD, CAT, and GSH-ox), effectively alleviating tumor hypoxia, depleting GSH, and breaking the antioxidant defense barrier. It is crucial that the Z-scheme heterojunctions greatly suppressed the recombination of electron-hole pairs under US excitation, maximizing the generation of cytotoxic ROS. Unlike the reported strategies of simply physically mixing or stacking different functional nanomaterials, our work constructs a Z-scheme heterojunction with tight contact and directional charge transfer paths through interface engineering, achieving deep integration and synergistic amplification of sonodynamic activity and multi-enzyme catalytic activity, rather than simple material combination. The synergistic effect of TME remodeling and ROS production disrupted the cellular redox homeostasis, leading to irreversible lipid peroxidation and induction of ferroptosis. This cascade reaction of oxidative damage and ferroptosis strongly triggered ICD, promoted DC maturation, and activated T cells. At the level of treatment mechanism, we not only utilize this sonodynamic catalytic system to achieve synergistic regulation of TME and ROS storm, but more importantly, the system reveals the intrinsic connection between sonodynamic catalytic amplification of ferroptosis effect and antitumor immune activation, thereby triggering ICD and cascading activation of systemic immune response. This sonodynamic catalysis-ferroptosis-immune activation cascade amplification mechanism is rarely reported in existing sonodynamic systems. Finally, the *in vivo* bilateral tumor model experiments demonstrated that CD@$FeV_2S_4$-mediated SDT/NCT can not only completely eradicate primary tumors, but also effectively inhibit the growth of distant untreated metastatic tumors, with good biological safety.

## Methods

### Preparation of $FeV_2S_4$ Nanoparticles

4 g of triethanolamine (Aladdin, China) was dispersed in 36 mL of deionized water, then 0.184 g of $Na_3VO_4$ (Aladdin, China), 0.405 g of $FeCl_3 \cdot 6H_2O$ (Aladdin, China) and 0.3 g of thioacetamide (Aladdin, China) were added in sequence. After stirring vigorously for 2 h, they were transferred to a hydrothermal reactor at 180 ℃ for 10 h of reaction. Following that, the product was subjected to multiple washes with deionized water and ethanol, and subsequently dried overnight in a vacuum oven.

### Preparation of CD

5 mg of indocyanine green (ICG) (Aladdin, China) was weighed and dispersed in 10 mL of anhydrous ethanol under ultrasonication to ensure complete dissolution. Subsequently, under vigorous stirring at room temperature, 1 mL of polyethylenimine ($M_W$ = 1800) (Aladdin, China) was added and the resulting solution was then subjected to a microwave reaction at 200 ° C for 10 min.

### Preparation of CD@$FeV_2S_4$ Heterojunctions

CDs and $FeV_2S_4$ nanoparticles were mixed in aqueous dispersion at a mass ratio of mCD:m$FeV_2S_4$ = 2:1 and stirred under dark conditions for 24 h to enable electrostatic self-assembly. The resulting CD@$FeV_2S_4$ heterojunctions were harvested by centrifugation, followed by three sequential washes with water and anhydrous ethanol to remove unbound CDs.

### Characterization

Images from a TEM and a high-resolution TEM were acquired using a JEOL-1400 and a JEOL-2100, respectively. The XPS analysis was carried out using a Kratos Axis Ultra DLD instrument. Cell-related staining experiments were conducted using Leica TCS SP5 laser confocal microscope. Beckman Cytoflex was utilized to perform flow cytometry analysis.

### Sonodynamic Performance Assessment

Aqueous dispersions of CD@$FeV_2S_4$ (0.1 mg/mL) were mixed with 60 μL of DPBF (Aladdin, China) solution (1 mg/mL) under dark condition. Then, ultrasonic treatment was carried out in the dark (50 kHz, 3.0 W/cm$^2$, 50% duty cycle). UV-vis absorption spectra were recorded every 1 min over 5 min, and the decay kinetics of DPBF absorbance at 421 nm were quantified to determine the initial $^1O_2$ generation rate. As a comparison, the same concentration of CD and $FeV_2S_4$ water solutions were tested under the same conditions. Additionally, by utilizing ESR spectroscopy, TEMP (Sigma) was employed as a selective scavenger for $^1O_2$ detection.

### Evaluation of POD-Like, GSH-ox-Like, and CAT-like Activities

100 μL of CD, $FeV_2S_4$, or CD@$FeV_2S_4$ aqueous solution (1 mg/mL) were respectively added to $H_2O_2$ acetate-sodium acetate (NaAc-HAc) buffer (pH 6.0, 6.5 or 7.4) in the presence of TMB (Aladdin, China). Following a designated incubation period, the absorbance of the sample solution at 652 nm,

indicative of the characteristic peak of oxidized TMB, was quantified using a UV-Vis spectrophotometer. Additionally, DMPO (Sigma) was selected as the •OH scavenger, and the POD-like activity of different materials to generate •OH was further determined by ESR spectroscopy.

DTNB (Aladdin, China) was selected as the indicator. 30 μL of 0.1 M GSH (Aladdin, China) was uniformly mixed with 3 mL of CD@$FeV_2S_4$ aqueous solution (100 μg/mL). At various time intervals, 300 μL of the mixed solution was sampled and combined with 10 μL of DTNB (10 mg/mL) and 2.7 mL of PBS buffer. The GSH consumption performance of CD@$FeV_2S_4$ was investigated by measuring the absorbance of the mixed solution at 412 nm. In addition, the GSH-ox-like activity of CD and $FeV_2S_4$ were also measured under the same conditions.

Deoxygenated $H_2O_2$ solutions of varying concentrations (10 mL, 0-0.4 mM) were mixed with a CD@$FeV_2S_4$ solution (1 mL, 100 μg/mL), and the generation of $O_2$ in the mixed solution was monitored using the dissolved oxygen meter. Concurrently, the CAT-like activities of CD and $FeV_2S_4$ were also evaluated under identical conditions.

## MTT Assay

NIH-3T3 and CT26 cells were purchased from Starfish Bioscience. The toxicity of CD@$FeV_2S_4$ on different cells was assessed using the MTT assay. Briefly, cells were seeded into 96-well plates with 5000-8000 cells per well. Upon completion of an overnight incubation, samples with diverse concentrations of CD, $FeV_2S_4$, and CD@$FeV_2S_4$ were introduced into the wells and co-incubated for 24 h.

## Live/Died and ROS Staining

Six-well plates were used to seed CT26 cells, which were then allowed to adhere overnight under standard culture conditions. Subsequently, cells were assigned to six experimental groups: Control, US, $FeV_2S_4$, CD@$FeV_2S_4$, $FeV_2S_4$ + US, CD@$FeV_2S_4$ + US. At the 4 h time point post-treatment initiation, US exposure was performed for all US-containing groups under standardized parameters. Following the full 24-hour post-treatment incubation, cells were harvested and stained with the Calcein AM/Propidium Iodide (PI) (Beyotime, China). Fluorescence images were acquired to assess live (green) and dead (red) cell populations. Intracellular ROS levels were quantified using the ROS Assay Kit (Beyotime, China).

## Western Blot Analysis

Following seeding of CT26 cells ($3 \times 10^5$) in six-well plates, a 24-hour incubation period was allowed. Upon completion of the designated treatments, cell lysis was carried out using RIPA lysis buffer with 1% PMSF. Protein concentrations were determined via a BCA assay, after which 20 μg protein samples were separated on SDS-PAGE and transferred onto PVDF membranes. Following blocking with 5% non-fat milk in Tris-buffered saline containing Tween 20 (TBST) for 1 hour at room temperature, membranes were washed with TBST and then subjected to overnight incubation at 4 °C with the appropriate primary antibodies. After washing with TBST, the membranes were incubated with the appropriate secondary antibodies for 2 h at room temperature. Subsequent to additional TBST washes, Western blot images were captured utilizing a digital gel imaging system.

## *In Vitro* ICD Marker Detection

Using an ATP detection kit (Beyotime, S0026) to detect ATP released from cells. Six-well plates were utilized to seed CT26 cells at a density of $2 \times 10^5$ cells per well, after which they were incubated overnight. The wells were then treated according to the experimental groups including Control, US, $FeV_2S_4$, CD@$FeV_2S_4$, $FeV_2S_4$ + US, and CD@$FeV_2S_4$ + US. Adherent cells were subsequently collected and assessed using the ATP assay kit. HMGB1 detection was performed similarly to ATP measurement, except that the supernatant from each well was analysed using an HMGB1 assay kit. CRT expression was evaluated by immunofluorescence staining. Cells were exposed to an anti-CRT primary antibody (Beyotime, AF1666, 1:500) for 3 hours at room temperature subsequent to washing. The cells were washed thrice with immunostaining wash buffer, then exposed to AF647-conjugated goat anti-rabbit IgG (Beyotime, A0468, 1:500) for 1 h. Following this, DAPI was introduced and allowed to incubate for 10 min. Subsequent to washing with PBS, the cells were imaged using confocal microscopy.

## *In Vitro* DC Maturation Detection

Under sterile conditions, we collected the humerus and tibia of mice. Subsequently, the bone marrow cavity was flushed using RPMI-1640 medium containing serum and double antibodies. GM-CSF and IL-4 with the concentration of 20 and 10 ng/mL were added the cells. Half of the medium was replaced on the third day, and all the medium was replaced and supplemented with fresh cytokines on the fifth day. On the 7th day, the suspended and semi adherent immature bone marrow mesenchymal stem cells were collected for experiments. Following seeding in 6-well plates at a density of $2 \times 10^5$ cells per well, CT26 cells in logarithmic growth phase were cultured overnight to encourage adhesion. After discarding the old medium, fresh medium containing different treatment

groups (Control, US, $FeV_2S_4$, CD@$FeV_2S_4$, $FeV_2S_4$ + US, CD@$FeV_2S_4$ + US) was added. For the groups involving US, after adding the materials, ultrasound equipment with a frequency of 50 kHz, intensity of 3.0 W/cm$^2$, and duty cycle of 50% was used for irradiation treatment. Subsequently, all well plates were incubated for another 24 h. Upon completion of the incubation period, the supernatant from each well containing CT26 cells was harvested, passed through a 0.22 μm filter to eliminate cellular debris, and subsequently combined with the BMDCs medium in a 1:1 volume ratio. The mixture was transferred to a 6-well plate with immature BMDCs. It was then incubated for an additional 24 hours at 37 °C with 5% $CO_2$ to stimulate DC maturation. Upon completion of the co-culture, retrieve all BMDCs from the 6-well plate by gentle pipetting. Subsequently, centrifuge the cells at 300×g for 5 minutes at 4 °C. Following discarding the supernatant, the cells underwent two washes with pre-cooled PBS. Following this, the cells were resuspended in 100 μL of flow cytometry buffer and subsequently incubated with a combination of fluorescent antibodies specific for CD11c-FITC (Biolegend, 117306, 1:200), CD80-PE (Biolegend, 104707, 1:200), and CD86-APC (Biolegend, 105011, 1:200). Subsequently, the cells were resuspended in 500 μL of buffer, filtered using a 40 μm cell strainer, and analyzed via flow cytometry. During analysis, the BMDC population was first gated using FSC-A/SSC-A, and then gated using $CD11c^+$. The proportions of $CD80^+$ and $CD86^+$ cells within this gate were counted to evaluate the induction effect of each treatment group on DC maturation.

## *In Vivo* Antitumor Therapy and Immunological Analysis

### (1) Construction of bilateral tumor models

The tumor model was established using BALB/c mice aged 5-7 weeks. Primary tumors were established by inoculating CT26 cells subcutaneously into the right flank of mice eight days before treatment. Prior to treatment, injection of CT26 cells was carried out at the left flank site to initiate distant tumor formation one day in advance. Intravenous injection of CD@$FeV_2S_4$ was administered on days 0, 2, and 4, followed by different treatments on days 1, 3, and 5. By day 7, all mice in each group were euthanized, and their main organs and blood samples were collected for histological section staining, blood routine examination, and blood biochemical testing. Additionally, tumor tissues were collected for H&E, TUNEL, and DHE histological section staining.

### (2) Immunological analysis

The euthanization of mice on day 7 led to the collection of lymph nodes, spleens, and tumor tissues to analyze dendritic cell maturation, T cell activation, and ICD markers. The supernatant of tumor tissue homogenates was analyzed for HMGB1 and ATP levels. Equal amounts of tumor tissue were processed identically. 500 μL of RIPA lysis buffer was added, followed by homogenization of tissues on ice. Upon homogenization, samples were centrifuged at 12,000 rpm for 15 minutes at 4 °C, resulting in the retrieval of the supernatant. The quantification of ATP levels was conducted with an ATP assay kit, and HMGB1 concentrations were determined employing ELISA. For the evaluation of DC and T cells, after sacrificing the mice, immerse them in 75% alcohol for 5 minutes for disinfection. On a sterile operating table, remove peripheral lymph nodes such as those from the inguinal and axillary regions, spleen, and tumor tissue, and place them in pre-cooled PBS. The lymph nodes and spleen are prepared into single-cell suspensions using a grinding method. The tissues are placed in a 200-mesh cell screen, gently ground with a tissue grinding rod until no visible lumps remain, and the screen is rinsed with PBS to collect the cell suspension. For tumor tissue, a mixed enzyme digestion method is used. The tumor is cut into pieces and added to a digestion solution containing collagenase and DNase I. It is digested in a shaker at 37° C for 1 to 2 hours, with observations made every 20 minutes to prevent overdigestion. After digestion is complete, all cell suspensions are filtered through a 200-mesh or 70 μm cell screen, centrifuged at 300 g for 5 minutes, and the spleen and tumor cell pellets are resuspended in 1× red blood cell lysis buffer. After lysing at room temperature for 2 to 3 minutes, PBS is added to terminate the lysis. After centrifugation again, the cells are resuspended in cell staining buffer and counted, and the cell concentration is adjusted to $1\times10^7$/mL for use. Single-cell suspensions were prepared from lymph nodes to evaluate dendritic cells (DCs). The cells were then stained with anti-CD11c-FITC (Biolegend, 117306, 1:200), anti-CD80-PE (Biolegend, 104707, 1:200), and anti-CD86-APC (Biolegend, 105011, 1:200) for subsequent flow cytometric analysis. Single-cell suspensions from spleens and tumors were stained with anti-CD3-FITC (Biolegend, 102023, 1:200), anti-CD4-APC (Biolegend, 100412, 1:200), and anti-CD8a-PE (Biolegend, 162304, 1:200) for T cell evaluation, followed by flow cytometry analysis. Additionally, primary and distant tumor tissues were collected for immunofluorescence staining.

### *In Vivo* Antitumor Efficacy Evaluation in Tumor Rechallenge Model

In order to evaluate the enduring immune memory response triggered by CD@$FeV_2S_4$ in conjunction with US, a tumor rechallenge model was established. BALB/C mice with CT26 tumors were segregated into two cohorts and administered intravenous injections of either PBS or CD@$FeV_2S_4$. The establishment of the tumor rechallenge model involved the injection of CT26 cells into the contralateral axilla of the mice on day 30. Five healthy mice were also utilized as the control group and were inoculated with CT26 cells in a similar manner. Spleens were retrieved on day 50 to assess the ratio of TEM ($CD3^+$) cells, notably $CD8^+$ T cells showing high CD44 levels and low CD62L levels. The spleen single-cell suspensions were subsequently stained with anti-CD3-FITC (Biolegend, 102023, 1:200), anti-CD8a-PE (Biolegend, 162304, 1:200), anti-CD44-PE-Cy7 (Biolegend, 103030, 1:200), and anti-CD62L-APC (Biolegend, 161218, 1:200), followed by analysis using flow cytometry.

### Statistical Analysis

The data represent the typical outcomes derived from a minimum of three independent experiments and are presented in the format of mean ± standard deviation. All statistical analyses were carried out utilizing Origin 2025 and Excel software. For multiple-group comparisons, one-way analysis of variance (ANOVA) was employed, whereas for two-group comparisons, a two-tailed Student's t-test was utilized. The levels of significance are denoted as follows: *$p < 0.05$, **$p < 0.01$, ***$p < 0.001$.

## Supplementary Material

Supplementary figures.
https://www.thno.org/v17p0604s1.pdf

## Acknowledgements

This work was supported by the China Anti-Cancer Association, Special Project for Discipline Construction of Standardized Myelosuppression Management (No. AHWJ2023BAc10039), the National Natural Science Foundation of China (No. 22278262), and the Science and Technology Commission of Shanghai Municipality (No. 25ZR1402150).

### Authorship Contributions

Yang Yang and Xiuwei Wu performed experiments and analyzed data. Zhenlin Zhang and Dengyu Pan provided suggestions for animal experiments. Bijiang Geng and Yunsheng Cheng contributed equally to funding acquisition, project administration and supervision. Bijiang Geng and Yunsheng Cheng wrote the original manuscript and edited the manuscript.

### Data availability statement

Data will be made available on request.

## Competing Interests

The authors have declared that no competing interest exists.

## References

1. Sun T, Zhang YS, Pang B, et al. Engineered Nanoparticles for Drug Delivery in Cancer Therapy. Angew Chem Int Ed. 2014; 53: 12320-12364.
2. Felfoul O, Mohammadi M, Taherkhani S, et al. Magneto-aerotactic bacteria deliver drug-containing nanoliposomes to tumour hypoxic regions. Nat Nanotechnol. 2016; 11: 941-947.
3. Petros RA, DeSimone JM. Strategies in the design of nanoparticles for therapeutic applications. Nat Rev Drug Discov. 2010; 9: 615-627.
4. Pan T, Zhang J, Wang X, Song Y. Global burden and trends of hematologic malignancies based on Global Cancer Observatory 2022 and Global Burden of Disease 2021. Exp Hematol Oncol. 2025; 14: 98.
5. Siegel RL, Wagle NS, Star J, et al. Colorectal cancer statistics, 2026. CA Cancer J Clin. 2026; 76: e70067.
6. Gonzalez PS, O'Prey J, Cardaci S, et al. Mannose impairs tumour growth and enhances chemotherapy. Nature. 2018; 563: 719-723.
7. Johnstone TC, Suntharalingam K, Lippard SJ. The Next Generation of Platinum Drugs: Targeted Pt(II) Agents, Nanoparticle Delivery, and Pt(IV) Prodrugs. Chem Rev. 2016; 116: 3436-3486.
8. Mansouri A, Ozair A, Bhanja D, et al. Stereotactic radiosurgery for patients with brain metastases: current principles, expanding indications and opportunities for multidisciplinary care. Nat Rev Clin Oncol. 2025; 22: 327-347.
9. Wang Y, Zhu N, Liu J, et al. Role of tumor microenvironment in ovarian cancer metastasis and clinical advancements. J Transl Med. 2025; 23: 539.
10. Liang XJ, Meng H, Wang Y, et al. Metallofullerene nanoparticles circumvent tumor resistance to cisplatin by reactivating endocytosis. P Natl Acad Sci USA. 2010; 107: 7449-7454.
11. Gong N, Ma X, Ye X, et al. Carbon-dot-supported atomically dispersed gold as a mitochondrial oxidative stress amplifier for cancer treatment. Nat Nanotechnol. 2019; 14: 379-387.
12. Pommier Y, Marchand C. Interfacial inhibitors: targeting macromolecular complexes. Nat Rev Drug Discov. 2011; 11: 25-36.
13. Sun S, Chen Q, Tang Z, et al. Tumor Microenvironment Stimuli-Responsive Fluorescence Imaging and Synergistic Cancer Therapy by Carbon-Dot-$Cu^{2+}$ Nanoassemblies. Angew Chem Int Edit. 2020; 59: 2-10.
14. Lin H, Chen Y, Shi J. Nanoparticle-triggered in situ catalytic chemical reactions for tumour-specific therapy. Chem Soc Rev. 2018; 47: 1938-1958.
15. Zhao L-P, Zheng R-R, Chen H-Q, et al. Self-Delivery Nanomedicine for $O_2$-Economized Photodynamic Tumor Therapy. Nano Lett. 2020; 20: 2062-2071.
16. Li X, Lovell JF, Yoon J, Chen X. Clinical development and potential of photothermal and photodynamic therapies for cancer. Nat Rev Clin Oncol. 2020; 17: 657-674.
17. Geng B, Hu J, Li Y, et al. Near-infrared phosphorescent carbon dots for sonodynamic precision tumor therapy. Nat Commun. 2022; 13: 5735.
18. Xiao L, Cai J, Wang Y, et al. Zr-Based Metal-Organic Framework Dual-Sensitized by Carbon Dot Sonosensitizers and $MnO_{2-x}$ Nanozymes for cGAS-STING Activation Enhanced Sonocatalytic-Immunotherapy. Adv Funct Mater. 2025; 36: e19998.
19. Cai J, Shen Q, Wu Y, et al. Defect Engineering of Biodegradable Sulfide Nanocage Sonozyme Systems Enables Robust Immunotherapy Against Metastatic Cancers. Adv Funct Mater. 2024; 34: 2411064.
20. Shen F, Tao D, Peng R, et al. Immunogenic nanomedicine based on GSH-responsive nanoscale covalent organic polymers for chemo-sonodynamic therapy. Biomaterials. 2022; 283: 121428.
21. He Y, Liu HS, Yin J, Yoon J. Sonodynamic and chemodynamic therapy based on organic/organometallic sensitizers. Coordin Chem Rev. 2021; 429: 213610.
22. Wu X, Liang J, Shu J, et al. Narrow-Bandgap Iridium(III)-$C_3N_5$ Nanocomplex as an Oxygen Self-Sufficient Piezo-Sonosensitizer for Hypoxic Tumor Sonodynamic Immunotherapy. J Am Chem Soc. 2025; 147: 15329-15343.
23. Chen H, He X, Zhou Z, et al. Metallic phase enabling $MoS_2$ nanosheets as an efficient sonosensitizer for photothermal-enhanced sonodynamic antibacterial therapy. J Nanobiotechnol. 2022; 20: 136.
24. Xu T, Zhao S, Lin C, et al. Recent advances in nanomaterials for sonodynamic therapy. Nano Res. 2020; 13: 2898-2908.
25. D'Autreaux B, Toledano MB. ROS as signalling molecules: mechanisms that generate specificity in ROS homeostasis. Nat Rev Mol Cell Biol. 2007; 8: 813-824.

26. Trachootham D, Alexandre J, Huang P. Targeting cancer cells by ROS-mediated mechanisms: a radical therapeutic approach? Nat Rev Drug Discov. 2009; 8: 579-591.
27. Brown JM, Wilson WR. Exploiting tumour hypoxia in cancer treatment. Nat Rev Cancer. 2004; 4: 437-447.
28. Wilson WR, Hay MP. Targeting hypoxia in cancer therapy. Nat Rev Cancer. 2011; 11: 393-410.
29. Xiong Y, Xiao C, Li Z, Yang X. Engineering nanomedicine for glutathione depletion-augmented cancer therapy. Chem Soc Rev. 2021; 50: 6013-6041.
30. Dai Y, Xu C, Sun X, Chen X. Nanoparticle design strategies for enhanced anticancer therapy by exploiting the tumour microenvironment. Chem Soc Rev. 2017; 46: 3830-3852.
31. Liu Y, Jiang Y, Zhang M, et al. Modulating hypoxia via nanomaterials chemistry for efficient treatment of solid tumors. Acc Chem Res. 2018; 51: 2502-2511.
32. Zhang P, Gao D, An K, et al. A programmable polymer library that enables the construction of stimuli-responsive nanocarriers containing logic gates. Nat Chem. 2020; 12: 381-390.
33. Ma L, Wang Y, Chen Y, et al. Optimizing the Electronic Structure of Iron Oxides via Nonmetallic Dopants for Enhanced Peroxidase Mimetic Catalysis. ACS Nano. 2025; 19: 28410-28421.
34. Wang D, Wu H, Wang C, et al. Self-Assembled Single-Site Nanozyme for Tumor-Specific Amplified Cascade Enzymatic Therapy. Angew Chem Int Ed. 2021; 60: 3001-3007.
35. Chen Y, Wang P, Hao H, et al. Thermal Atomization of Platinum Nanoparticles into Single Atoms: An Effective Strategy for Engineering High-Performance Nanozymes. J Am Chem Soc. 2021; 143: 18643-18651.
36. Wang Z, Li Z, Sun Z, et al. Visualization nanozyme based on tumor microenvironment "unlocking" for intensive combination therapy of breast cancer. Sci Adv. 2020; 6: eabc8733.
37. Zhong X, Wang X, Cheng L, et al. GSH-depleted $PtCu_3$ nanocages for chemodynamic-enhanced sonodynamic cancer therapy. Adv Funct Mater. 2020; 30: 1907954.
38. Jing X, Meng L, Fan S, et al. Tumor microenvironment self-regulation: Bimetallic metal nanozyme-derived multifunctional nanodrug for optimizable cascade catalytic reaction-synergetic anti-tumor theranostics. Chem Eng J. 2022; 442: 136096.
39. Su Y, Wu F, Song Q, et al. Dual enzyme-mimic nanozyme based on single-atom construction strategy for photothermal-augmented nanocatalytic therapy in the second near-infrared biowindow. Biomaterials. 2022; 281: 121325.
40. Dong S, Dong Y, Zhao Z, et al. "Electron Transport Chain Interference" Strategy of Amplified Mild-Photothermal Therapy and Defect-Engineered Multi-Enzymatic Activities for Synergistic Tumor-Personalized Suppression. J Am Chem Soc. 2023; 145: 9488-9507.
41. Ma Z, Foda MF, Liang H, et al. In Situ Nanozyme-Amplified NIR-II Phototheranostics for Tumor-Specific Imaging and Therapy. Adv Funct Mater. 2021; 31: 2103765.
42. Tang J, Zhang X, Cheng L, et al. Multiple stimuli-responsive nanosystem for potent, ROS-amplifying, chemo-sonodynamic antitumor therapy. Bioact Mater. 2022; 15: 355-371.
43. Wu J, Sha J, Zhang C, et al. Recent advances in theranostic agents based on natural products for photodynamic and sonodynamic therapy. View. 2020; 1: 20200090.
44. Geng B, Zhang S, Yang X, et al. $Cu_{2-x}O@TiO_{2-y}$ Z-scheme heterojunctions for sonodynamic-chemodynamic combined tumor eradication. Chem Eng J. 2022; 435: 134777.
45. Hu J, He X, Cai J, et al. Biodegradable $CoSnO_3$ nanozymes modulate pH-responsive graphene quantum dot release for synergistic chemo-sonodynamic-nanocatalytic cancer therapy. Chem Eng J. 2024; 481: 148561.
46. Li Y, Jia W, Zhu M, et al. Focused Acoustic Vortex-Activated Dual-Stimuli Nanoplatform Synergizes with Checkpoint Blockade to Enhance Macrophage Phagocytosis and Antitumor Immunity. ACS Nano. 2025; 19: 27957-27976.
47. Yu N, Ding M, Wang F, et al. Near-infrared photoactivatable semiconducting polymer nanocomplexes with bispecific metabolism interventions for enhanced cancer immunotherapy. Nano Today. 2022; 46: 101600.
48. Li J, Yu X, Jiang Y, et al. Second Near-Infrared Photothermal Semiconducting Polymer Nanoadjuvant for Enhanced Cancer Immunotherapy. Adv Mater. 2021; 33: 2003458.
49. Zhang Z, Yue YX, Li Q, et al. Design of Calixarene-Based ICD Inducer for Efficient Cancer Immunotherapy. Adv Funct Mater. 2023; 33: 2213967.
50. Zheng RR, Zhao LP, Huang CY, et al. Paraptosis Inducer to Effectively Trigger Immunogenic Cell Death for Metastatic Tumor Immunotherapy with IDO Inhibition. ACS Nano. 2023; 17: 9972-9986.
51. Liu M, Liu B, Liu Q, et al. Nanomaterial-induced ferroptosis for cancer specific therapy. Coordin Chem Rev. 2019; 382: 160-180.
52. Wang M, Zhang W, Liu B, et al. Boosting Cancer Cell Ferroptosis with Carbon Monoxide Poisoned Hemoglobin. J Am Chem Soc. 2025; 147: 17372-17383.
53. Li J, Yang S, Deng Y, et al. Emancipating target-functionalized carbon dots from autophagy vesicles for a novel visualized tumor therapy. Adv Funct Mater. 2018; 28: 1800881.
54. Zhao J, Cai J, Hu J, et al. Biodegradable hollow $MnO_2$ decorated by carbon dots with cholesterol depletion capability for cascaded amplification of sono-immunotherapy. Biomaterials. 2025; 325: 123559.
55. Zeng L, Ding S, Cao Y, et al. A MOF-Based Potent Ferroptosis Inducer for Enhanced Radiotherapy of Triple Negative Breast Cancer. ACS Nano. 2023; 17: 13195-13210.
56. Feng W, Liu Z, Xia L, et al. A Sonication-Activated Valence-Variable Sono-Sensitizer/Catalyst for Autography Inhibition/Ferroptosis-Induced Tumor Nanotherapy. Angew Chem Int Ed. 2022; 61: e202212021.
57. Liu B, Chen X, Zhu Y, et al. One-Step Symbiosis of Bimetallic Peroxides Nanoparticles to Induce Ferroptosis/Cuproptosis and Activate cGAS-STING Pathway for Enhanced Tumor Immunotherapy. Adv Mater. 2025; 37: 2500337.
58. You C, Li X, Wang D, et al. Self-Assembled Aza-Boron-Dipyrromethene for Ferroptosis-Boosted Sonodynamic Therapy. Angew Chem Int Ed. 2022; 61: e202210174.
59. Zhan M, Wang F, Liu Y, et al. Dual-Cascade Activatable Nanopotentiators Reshaping Adenosine Metabolism for Sono-Chemodynamic-Immunotherapy of Deep Tumors. Adv Sci. 2023; 10: 2207200.
60. Qi J, Jia S, Kang X, et al. Semiconducting Polymer Nanoparticles with Surface-Mimicking Protein Secondary Structure as Lysosome-Targeting Chimaeras for Self-Synergistic Cancer Immunotherapy. Adv Mater. 2022; 34: 2203309.
61. Liu XZ, Wen ZJ, Li YM, et al. Bioengineered Bacterial Membrane Vesicles with Multifunctional Nanoparticles as a Versatile Platform for Cancer Immunotherapy. ACS Appl Mater Interfaces. 2023; 15: 3744-3759.
62. Long X, Wang H, Yan J, et al. Tailor-Made Autophagy Cascade Amplification Polymeric Nanoparticles for Enhanced Tumor Immunotherapy. Small. 2023; 19: 2207898.
63. Wang S, Huang P, Chen X. Hierarchical targeting strategy for enhanced tumor tissue accumulation/retention and cellular internalization. Adv Mater. 2016; 28: 7340-7364.
64. Chen Q, Chen M, Liu Z. Local biomaterials-assisted cancer immunotherapy to trigger systemic antitumor responses. Chem Soc Rev. 2019; 48: 5506-5526.
65. Shao D, Zhang F, Chen F, et al. Biomimetic Diselenide-Bridged Mesoporous Organosilica Nanoparticles as an X-ray-Responsive Biodegradable Carrier for Chemo-Immunotherapy. Adv Mater. 2020; 32: 2004385.
66. Meng Z, Zhang Y, She J, et al. Ultrasound-Mediated Remotely Controlled Nanovaccine Delivery for Tumor Vaccination and Individualized Cancer Immunotherapy. Nano Lett. 2021; 21: 1228-1237.
67. Sun X, Zhang Y, Li J, et al. Amplifying STING activation by cyclic dinucleotide–manganese particles for local and systemic cancer metalloimmunotherapy. Nat Nanotechnol. 2021; 16: 1260-1270.
68. Yang Z, Zhu Y, Dong Z, et al. Tumor-killing nanoreactors fueled by tumor debris can enhance radiofrequency ablation therapy and boost antitumor immune responses. Nat Commun. 2021; 12: 4299.